Case Studies in Thermal Engineering 81 (2026) 108042

Contents lists available at ScienceDirect

Case Studies in Thermal Engineering

journal homepage: www.elsevier.com/locate/csite

Numerical study on unsteady heat transfer characteristics of phase change plates optimized by fin structure

Shiyu Liao [a], Xiang Li [a], Jiri Zhou [b], Xiaoyan Yi [c], Ruiyong Mao [a], Hongwei Wu [d], Zujing Zhang [a,*]

[a] College of Civil Engineering, Guizhou University, Guiyang, 550025, China
[b] Chengdu Laboratory for Innovation and Application of Low-Carbon Intelligent Building- Management Systems, China MCC5 Group CORP.LTD, Chengdu, 610000, China
[c] The Hong Kong Polytechnic University Department of Building Environment and Energy Engineering, China
[d] School of Physics, Engineering and Computer Science, University of Hertfordshire, Hatfield, AL10 9AB, United Kingdom

GRAPHICAL ABSTRACT

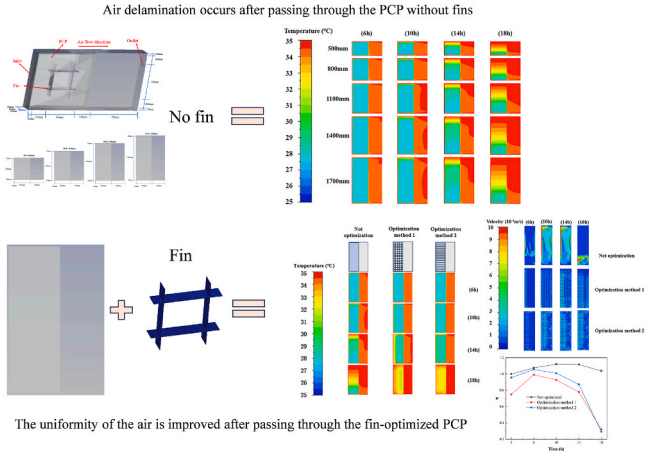

ARTICLE INFO

Keywords:
Phase change plates
Melt stratification

ABSTRACT

The energy crisis has heightened the importance of phase change energy storage technology as a key enabler for orderly energy transformation. However, the density variation of phase change materials during phase transition is often overlooked, leading to issues such as reduced heat

* Corresponding author.
E-mail address: zjzhang3@gzu.edu.cn (Z. Zhang).

https://doi.org/10.1016/j.csite.2026.108042
Received 10 November 2025; Received in revised form 6 March 2026; Accepted 7 April 2026
Available online 8 April 2026

Fin structure
Performance optimization

transfer efficiency and local overheating. In previous studies, the inhibition effect of phase transition stratification has been found as an incidental result of thermal performance studies. There are few studies have systematically analyzed it. Therefore, in this study, the fin structure is studied by numerical simulation to mitigate the resulting stratification phenomenon. The results can reduce the thermal efficiency loss of the phase change plate and the risk of local overheating of the system. Specifically, the inhibitory effects of fin length, the number of transverse fins, and the presence of longitudinal fins on melting stratification are analyzed. The phase change plate melting rate is calculated as the total melting mass divided by the total melting time. The melting uniformity of the phase change plate was determined by the liquid phase component gradient. The temperature inhomogeneity coefficient is used to determine the air uniformity after passing through the phase change plate. The main results are as follows: (1) The plain phase change plate (without fins) showed an abrupt temperature rise followed by stabilization during melting, with a concurrent shift in its liquid fraction curve; (2) Increases in fin length, transverse fin number, and longitudinal fin number all improved the plate's melting rate and temperature uniformity, with maximum improvements of 10.86% and 293%, respectively; (3) The PCP of the optimized method 1 has better melting uniformity, but the initial cost is higher than that of the optimized method 2.

Nomenclature

Greek symbols		S_ε	Turbulent dissipation term (W/kg)
μ	Dynamic viscosity coefficient (Pa·s)	f_{up}	Liquid fraction of the upper part of the phase change plate
β	Coefficient of volumetric expansion ($°C^{-1}$)	δ_{zi}	Kronecker operator
u, v, ω	The speed is a sub-velocity in different directions (m/s)	f_{down}	Liquid fraction of the lower part of the phase change plate (°C)
θ	Liquid phase component gradient	$T_{\max}$	The maximum temperature of the cross-section (°C)
η	Temperature inhomogeneity coefficient	$T_{\min}$	The minimum temperature of cross-section (°C)
Subscripts		T_{ave}	The average temperature of cross-section (°C)
G_k	The turbulent energy term produced by the laminar velocity gradient (W/kg)	*Abbreviations*	
G_b	Turbulent energy produced by buoyancy (W/kg)	PCM	Phase change materials
Y_M	Contribution of turbulent pulsating expansion to the rate of dissipation (W/kg)	PCP	phase change plates
C_1, C_2, C_3	Constant	FL	Fin length
S_k	Turbulent energy term (W/kg)	NOTF	Number of transverse fins
S_ε	Turbulent dissipation term (W/kg)	NOLF	Number of longitudinal fins

1. Introduction

A variety of reasons have led to the global tight energy supply and soaring prices, making it difficult for hundreds of millions of people to bear the heavy cost of living and pushing them into extreme poverty [1]. As an important cornerstone of national development, energy holds a significant strategic position [1]. In the current context where geopolitical risks are intensifying and energy security is severely affected, carrying out a reasonable and orderly energy transition and optimizing the energy structure is one of the good solutions [2,3].

Amid the global energy transition wave, phase change energy storage technology has stood out with its unique physical properties and application potential, becoming an important breakthrough in solving the energy storage problem [4]. The core advantage of PCM is its ability to efficiently store and release latent heat through phase change processes such as solid-liquid [5], solid-solid [6], and liquid-gas [7]. Compared with traditional sensible heat storage and chemical heat storage, the energy storage density of phase change materials (PCM) can be more than 5 times that of sensible heat storage [4,8,9]. It can also keep the temperature constant during the phase change process, which significantly improves the energy efficiency [10,11]. This property makes it show great potential in the fields of solar heat storage [12], building energy efficiency [13], and industrial waste heat recovery [14] [15]. In addition, PCM has a long lifespan, high safety, and environmental friendliness, and its physical energy storage mechanism avoids the risk of flammability and explosion in chemical reactions, and the materials are non-toxic and recyclable, which meets the core requirements of green development [16,17].

In specific applications, PCM multi-scenario adaptability further strengthens its advantages. In the construction sector, PCM can be integrated into floors [18], walls [19], glazing [20], roofs [17]and even building materials [21] to save energy or reduce indoor temperatures. In the field of electronic devices, PCM is widely used in thermal management of mobile phones [22], laptops, electric vehicles [23], and data centers [24]. In the field of refrigeration equipment, PCM is widely used in refrigerated display cabinets [25] beverage refrigerated cabinets [26], air conditioning systems [27], and refrigerated warehouses. In the field of wearable devices, PCM is used to maintain the surface microambient temperature of the head [28], face [29], trunk [30], and joints [31,32] to reduce the adverse effects of improper application of heat energy on human health. Despite the promising prospects of PCM, their practical application encounters significant challenges. A key issue stems from the density difference between the solid and liquid phases of the

material.

Li et al. [33] found that the melting process of PCM was uneven due to the different densities before and after melting. In addition, this phenomenon was also observed in the study of Gao et al. [34]. This disparity can lead to phase separation during operation, resulting in problems such as reduced heat transfer efficiency, local overheating, and even complete failure of the phase change process. In a study conducted by Ahmed Said et al. [35], the incorporation of eight external fins on the casing of a high-enthalpy shell-and-multi-tube phase change material (PCM) thermal storage system was found to enhance heat transfer while simultaneously suppressing melting and delamination. Similarly, Hong et al. [36] adopted a combined approach utilizing fins and separators to improve the thermal performance of photovoltaic-PCM systems, which also proved effective in mitigating melting and delamination. Wang et al. [37] demonstrated that layered fins are particularly effective in guiding heat transfer pathways within thermal energy storage units. Meanwhile, Mahdi et al. [38] proposed a spiral coil shell storage system integrated with a novel central return pipe, which was shown to enhance heat transfer efficiency and partially alleviate melting-induced delamination. Abdellatif et al. [39] investigated PCM encapsulation geometries—specifically truncated and tapered configurations to address issues of thermal stratification and melting behavior. Their results indicated that tanks employing conical and truncated conical containers can effectively mitigate thermal stratification. In summary, structural optimizations involving fins and encapsulation design are viable strategies for preventing PCM delamination during melting processes. Waqas et al. [40] double performance improvements are achieved through optimized configurations: 10.07% faster melt time for narrower thermal designs and 13.65% better temperature uniformity compared to eccentric heating configurations.

Fin structures are commonly employed to enhance heat transfer within thermal systems. For instance, Danışmaz [41] examined the influence of fin cross-sectional geometry on the thermal-hydraulic performance of a pin-fin heat sink under turbulent conditions, demonstrating that an elliptical fin with an aspect ratio of 0.50 could enhance the heat transfer rate significantly, improving the thermal performance factor by 90% compared to a conventional circular design. Jaberi et al. [42] replaced solid fins with porous fins at various locations within an latent heat thermal energy storage system, reporting a reduction in total melting time by up to 21% and a corresponding increase in storage power of 26.6%. In the context of printed circuit heat exchangers, Bhowmik et al. [43] arranged a PCM in a shell-and-tube configuration with external fins, achieving a 53.10% reduction in melting time compared to a finless configuration; a rectangular fin arrangement also exhibited the highest heat transfer rate of 2040.83 W. Zhou et al. [44] incorporated copper foam fins and solid copper fins into spherical PCM capsules within a packed-bed latent heat thermal energy storage system. Their results showed that copper foam fins significantly accelerated heat transfer, reducing charging and discharging times by 29.7% and 59.5%, respectively, compared to finless capsules. Guo et al. [45] added external fins to an ice-based latent heat storage device, observing a 34.12% improvement in cooling efficiency and a 9.3% increase in melting rate. Waqas et al. [46] found that when fins are used with hybrid nanoparticles, the total melting rate of PCM is about 41% faster. In addition to this, Waqas et al. [47] considered the effectiveness of fin geometry and different fin angles in rectangular cavities. Khalid et al. [48] integrated nanoparticles with novel fractal H-shaped solid fins, which can increase the melting rate by up to 60%. Zainab et al. [49] integrated nanoparticles and V-shaped fins into the PCM, and the results showed that energy storage was increased by 5.43%. Shahraki et al. [50] integrated longitudinal scatter and alumina nanoparticles into PCMs to explore a three-tube latent thermal energy storage system, and found that 64 heat sinks with a thickness of 125 μm reduced the charging time by 86% compared with the basic situation without scatter. Tavakoli et al. [51] studied the solid-liquid phase transition of PCM in a rectangular shell with corrugated fins, and developed an alternative model to optimize the fin geometry based on artificial neural networks combined with particle swarm optimization. The optimized geometry compared to the planar fins can improve the thermal energy storage efficiency ratio per unit mass by 43%.

It is established that fin structures serve the dual purpose of enhancing heat transfer and suppressing the stratification of PCM. Nevertheless, the inhibitory effect of fins on delamination has typically been a corollary finding in research focused on thermal performance, with a systematic analysis of the mechanism still absent. Due to the excellent temperature control performance and easy installation of phase change plate (PCP), they have been widely applied in data centers [52], underground refuge chambers [53], building energy storage [54], and other fields. However, PCP is prone to stratification, and its dynamics and mitigation need urgent research. Li et al. [55] observed that melting and stratification were alleviated when fractal fins were applied to photovoltaic-phase change systems. However, the research focuses on the temperature uniformity of photovoltaic panels, rather than the in-depth analysis and optimization of the melting and stratification mechanism within the PCP. Tu et al. [56] enhanced the melting uniformity of PCM by introducing array heat exchanger tubes. However, this method increases the complexity and cost of the system, and does not clearly explain the reconstruction effect of its structure on natural convection morphology. Xu et al. [57] achieved a 93% improvement in melting uniformity through structural optimization, indicating that structural design has a key impact on uniformity. However, his research did not specifically focus on the specific physical problem of melting stratification dominated by strong natural convection in PCP. Existing research on enhancing PCP mainly focuses on improving the overall heat transfer rate or temperature uniformity. However, there is still a lack of research on the use of simple and fabricable fin structures to inhibit significant melt stratification caused by buoyancy-driven natural convection in PCPs. Therefore, it is of practical significance to study hierarchical inhibition by optimizing fin layout.

Complex fin geometries tend to excel in improving average heat transfer rates. However, this extreme pursuit of heat transfer rates can sometimes exacerbate local flow inequalities or create new flow dead zones. It may not be conducive to solving the problem of stratification. The simple orthogonal layout of this study shows unique advantages in achieving fundamental homogenization of the temperature field by clearly dividing the flow region and establishing regular thermal conductivity paths. By introducing a fin-optimized stainless steel encapsulated PCP, the key gap in PCP layering problem is directly addressed. It moves beyond the incidental findings of previous heat transfer studies to systematically demonstrate that the internal fins control the flow field. The findings not only confirm the efficacy of fins in suppressing stratification but also provide mechanistic insights that mitigate risks of efficiency

loss and local overheating, thereby enhancing system reliability.

2. Methodology

2.1. Physical model and mesh

2.1.1. Physical model

This study employs numerical simulation to optimize the heat transfer performance of a PCP by investigating the size and number of its support fins. To reduce computational cost, a simplified numerical model was adopted. The Foundation physical model, illustrated in Fig. 1(a), consists of a main chamber (1120 mm in length, 100 mm in width, and 540 mm in height) containing a PCP with dimensions of 600 mm × 500 mm × 60 mm. In addition, this study also investigated the heat transfer stratification phenomena of PCPs at different heights. The physical models with PCPs of different heights are shown in Fig. 1(b). The only difference between these models and the basic model is the different heights of the main chamber and the PCP. The computational domain is divided by the PCP shell and fins into three distinct regions: the air-filled space between the chamber wall and the PCP housing, the PCM contained within the PCP housing and around the fins, and the stainless steel comprising the fins and the PCP shell itself. Hot air is forced through the PCP from the inlet to the outlet.

2.1.2. Mesh and grid independence

A simplified numerical model for optimizing the convective heat transfer of the PCP was developed using ICEM. The model comprises three computational domains: the air flow domain, the PCM thermal storage domain, and the fin-enhanced heat transfer domain. Coupling boundaries were defined at the interfaces between these domains, specifically at the PCP shell separating the air flow from the PCM, and at the interface between the PCM and the fins. To minimize numerical error at these interfaces and to accurately resolve the PCM melting process and the fins' role in heat transfer enhancement, the mesh was locally refined around the PCP and the supporting fins, as illustrated in Fig. 2. This method was used for all subsequent model meshes.

In order to verify the grid independence, we systematically investigated the effects of five different mesh numbers (2×10^5, 4×10^5, 7×10^5, 8×10^5 and 10×10^5) on the calculation results. For time step independence, we systematically investigated the effects of five different time steps (1s, 2s, 5s, 8s, and 10s) on the calculation results. Since the ambient temperature and supply air speed only affect

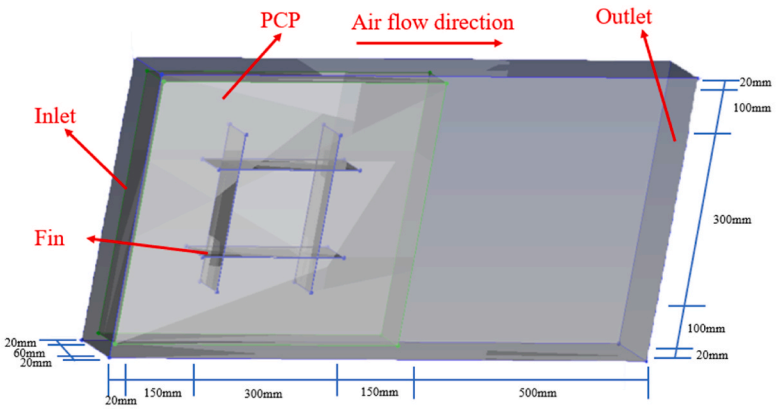

(a)

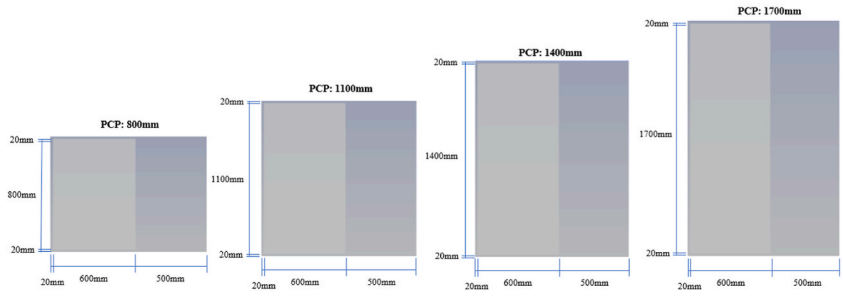

(b)

Fig. 1. PCP optimized physical model for heat transfer performance: (a) Foundation physical model; (b) PCP models of different heights.

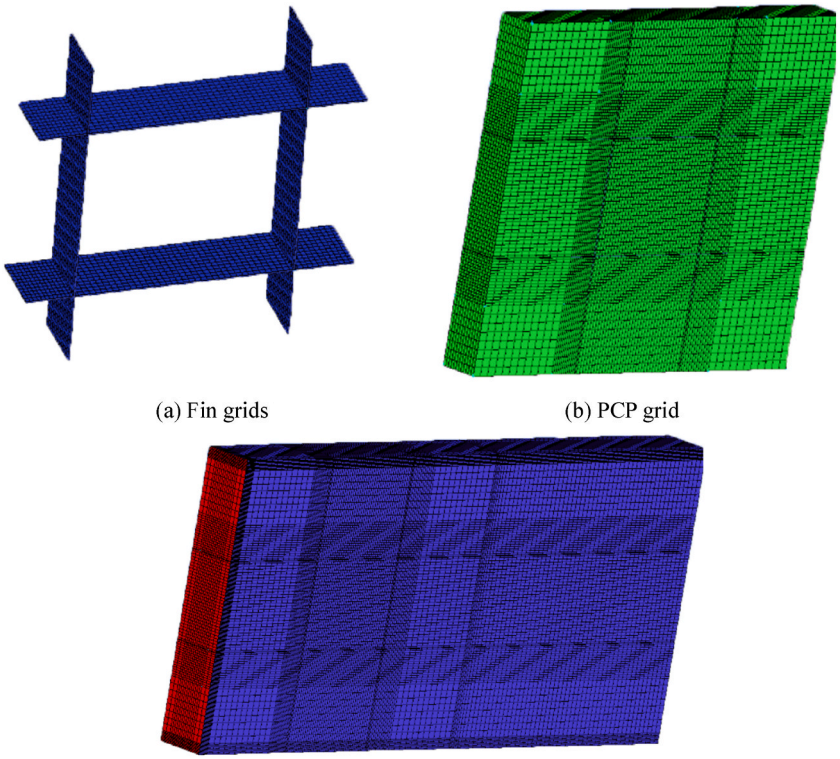

Fig. 2. Grid details.

the heat transfer time, not the PCP melt stratification. In order to save the time cost of the calculation, the ambient temperature was set to 35 °C, the supply air speed was set to 1.8 m/s, the encapsulation material and fin material were set to stainless steel, and the paraffin wax was set to PCM, and the settings were consistent with the experiment. When the residuals of the continuity equation, momentum equation, k-value, and e value $\leq 10^{-3}$, and the residual of the energy equation $\leq 10^{-6}$, the solution is considered convergent. As shown in Fig. 3(a), the liquid fraction of PCP during 12 h of heating showed a significant difference when the number of grids was less than 7 $\times$ 10^5. When the number of meshes exceeds this value, the liquid fraction stabilizes. Therefore, the number of meshes of 7 $\times$ 10^5, was used to calculate the subsequent numerical simulations to ensure the balance between the calculation accuracy and the calculation efficiency. As shown in Fig. 3(b), when the grid time step number is less than 5 s, the liquid phase fraction of PCP during 12 h of heating shows a significant difference. When the number of meshes exceeds this value, the liquid phase fraction stabilizes. Therefore, the time step of 5s is used to calculate the subsequent numerical simulation to ensure the balance between computational accuracy and computational efficiency.

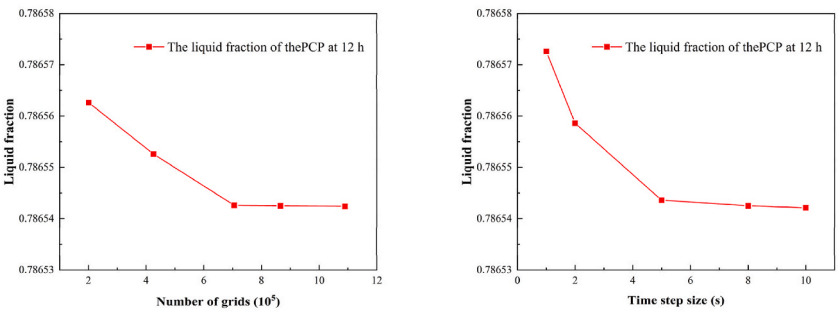

Fig. 3. Verification of grid independence.

2.2. CFD model

2.2.1. Viscosity model

The heat transfer process was simulated using the solidification/melting model coupled with the standard k-ε turbulence model and enhanced wall treatment. This approach is justified by the work of Gao et al. [58], who showed that this model combination yields results in good agreement with experimental data for similar PCP-air systems. For LES models, their computational costs are extremely high, and the requirements for mesh and transient solvers are far beyond the practical scope of engineering. It is not suitable for long-term transient phase change coupling simulations in this study. For the RSM model, its equations are complex and the solution stability is poor. It is difficult to converge in the coupling problem of strong buoyancy and phase change. And the computational overhead is much greater than that of the standard k−ε model. For the k−ω SST model, although it performs well in the near-wall zone and separation flow prediction, it is more sensitive to the inlet turbulence parameter. Moreover, the computational efficiency of the turbulent core area is lower than that of the k−ε model. For k−ε RNG and Realizable models, the accuracy is slightly improved in some flows. However, the improvement is mainly reflected in the strong swirl or high strain rate area, and the gain of the fully developed channel flow led by this study is limited. However, it increases the complexity and convergence uncertainty of the model. Therefore, the standard k-ε turbulence model and enhanced wall treatment was also used in this study. The transport equations for k and ε are presented below [59]:

$$\frac{\partial}{\partial \tau}(\rho k)+\frac{\partial}{\partial x_i}(\rho k u_i)=\frac{\partial}{\partial x_j}\left[\alpha_k \mu_{eff}\frac{\partial k}{\partial x_j}\right]+G_k+G_b-\rho\varepsilon-Y_M+S_k \tag{1}$$

$$\frac{\partial}{\partial \tau}(\rho \varepsilon)+\frac{\partial}{\partial x_i}(\rho \varepsilon u_i)=\frac{\partial}{\partial x_j}\left[\alpha_\varepsilon \mu_{eff}\frac{\partial \varepsilon}{\partial x_j}\right]+C_{1\varepsilon}\frac{\varepsilon}{k}(G_k+C_{3\varepsilon}G_b)-C_{2\varepsilon}\rho\frac{\varepsilon^2}{k}-R_\varepsilon+S_\varepsilon \tag{2}$$

Where, G_k denotes the turbulent energy term resulting from laminar velocity gradients; G_b is the term for turbulent energy resulting from buoyancy; Y_M denotes the contribution of turbulent pulsating expansion to the dissipation rate of the entire process in compressible flow. In incompressible flow, C_1 C_2, and C_3 are constants, $C_1 = 1.44$, $C_2 = 1.92$, $C_3 = 0$; S_k and S_ε are the user-defined turbulent energy terms and turbulent dissipation terms, $S_k = 0$, $S_\varepsilon = 0$.

2.2.2. Governing equations

Numerical simulation can effectively solve the problem that the melting and heat transfer characteristics of PCM cannot be visualized during the experiment. The enthalpy-porosity model is a reliable method to capture changes in the condensation-melting interface and is widely used to solve the problem of solidification and thawing [45]. Therefore, the phase change process in this study is modeled using the enthalpy-porosity method.

In the current numerical simulation, in order to simplify the model, several assumptions are made [10].

(1) The liquid is a Newtonian fluid and is incompressible. This assumption is based on the low flow velocity and low Mach number flow conditions of PCM and air in this study. Among them, the shear stress has a linear relationship with the strain rate, and the density change is mainly driven by temperature. A standard and well-proven engineering simplification for simulating such forced/natural convection heat transfer problems;
(2) Ignoring the volume change of PCM during the melting process [60]. In rigidly packaged PCPs, the volume change caused by the phase transition is constrained. Its influence on the dominant heat transfer mechanism and macroscopic melting mode is a second-order effect, so it can be ignored within the engineering accuracy;
(3) The air is dry air. In forced convection cooling applications, air humidity has little effect on the heat transfer coefficient. Therefore, the use of dry air and incompressible assumptions is a widely accepted standard engineering simplification in this field;
(4) PCM are incompressible and isotropic. For industrial-grade paraffin PCMs that are uniformly encapsulated and have no directional crystallization. Its isotropy and incompressibility hypothesis are standard and physically reasonable simplifications for analyzing its macroscopic thermal-current coupling behavior.

Given the significant non-isothermal temperature changes and resultant density variations in the air flow, the Boussinesq approximation is applied. This approximation assumes negligible viscous dissipation and constant thermophysical properties except for density. The corresponding Navier-Stokes equations are [61]:

$$\frac{\partial u_i}{\partial \tau}+u_j\frac{\partial u_i}{\partial x_j}=-\frac{1}{\rho}\frac{\partial p}{\partial x_i}+\frac{\partial}{\partial x_j}\left[\mu\left(\frac{\partial u_i}{\partial x_j}+\frac{\partial u_j}{\partial x_i}\right)\right]+g\beta\Delta T\delta_{zi} \tag{3}$$

Where, μ is the dynamic viscosity coefficient (N·s/m^2), β is the coefficient of volumetric expansion, δ_{zi} is a Kronecker operator, g is the acceleration due to gravity (m/s^2).

The equation for conservation of mass is [62]:

$$\rho_f\left(\frac{\partial u}{\partial x}+\frac{\partial v}{\partial y}+\frac{\partial w}{\partial z}\right)=0 \tag{4}$$

The equation for the conservation of momentum is [62]:

$$\rho_f\left[\frac{\partial u}{\partial t}+\frac{\partial(uu)}{\partial x}+\frac{\partial(uv)}{\partial y}+\frac{\partial(uw)}{\partial z}\right]=\left[\frac{\partial}{\partial x}\left(\mu\frac{\partial u}{\partial x}\right)+\frac{\partial}{\partial y}\left(\mu\frac{\partial u}{\partial y}\right)+\frac{\partial}{\partial z}\left(\mu\frac{\partial u}{\partial z}\right)\right]-\frac{\partial p}{\partial x} \tag{5}$$

$$\rho_f\left[\frac{\partial v}{\partial t}+\frac{\partial(vu)}{\partial x}+\frac{\partial(vv)}{\partial y}+\frac{\partial(vw)}{\partial z}\right]=\frac{\partial}{\partial x}\left(\mu\frac{\partial v}{\partial x}\right)+\frac{\partial}{\partial y}\left(\mu\frac{\partial v}{\partial y}\right)+\frac{\partial}{\partial z}\left(\mu\frac{\partial v}{\partial z}\right)\Big]-\frac{\partial p}{\partial y} \tag{6}$$

$$\rho_f\left[\frac{\partial w}{\partial t}+\frac{\partial(wu)}{\partial x}+\frac{\partial(wv)}{\partial y}+\frac{\partial(ww)}{\partial z}\right]=\left[\frac{\partial}{\partial x}\left(\mu\frac{\partial w}{\partial x}\right)+\frac{\partial}{\partial y}\left(\mu\frac{\partial w}{\partial y}\right)+\frac{\partial}{\partial z}\left(\mu\frac{\partial}{\partial z}\right)\right]-\frac{\partial p}{\partial z} \tag{7}$$

The equation for conservation of energy is [62]:

$$\rho_f\left[\frac{\partial T_f}{\partial t}+\frac{\partial(T_f u)}{\partial x}+\frac{\partial(T_f v)}{\partial y}+\frac{\partial(T_f w)}{\partial z}\right]=\frac{\partial}{\partial x}\left(\frac{k}{c_f}\frac{\partial T_f}{\partial x}\right)+\frac{\partial}{\partial y}\left(\frac{k}{c_f}\frac{\partial T_f}{\partial y}\right)+\frac{\partial}{\partial z}\left(\frac{k}{c_f}\frac{\partial T_f}{\partial z}\right)+S_T \tag{8}$$

The phase transformation model is numerically simulated by the mathematical enthalpy porosity model. The thickness of the melting zone in this study is about 1/5, which belongs to the category of thin melting zone. According to the conclusion of Ebrahimi et al. [63], heat conduction under the thin melt zone is the dominant heat transfer mode in the melting region, and the contribution of convective heat transfer is low. Therefore, when mushy zone constant $\geq 10^5$, the sensitivity of numerical predictions to values is negligible. Where mushy zone constant is set to 10^5 [64]. The enthalpy model is as follows [65]:

$$\rho\frac{\partial H}{\partial t}=\lambda\nabla^2 T \tag{9}$$

H is calculated by the following formula [65]:

$$H=h+\beta L \tag{10}$$

$$h=h_{ref}+\int_{T_{ref}}^{T}C_p dT \tag{11}$$

The latent enthalpy H is related to the liquid composition β is defined using the following [65]:

$$\beta=\begin{cases}0 & T<T_{m1}\\ \dfrac{T-T_{m1}}{T-T_{m2}} & T_{m1}\leq T\leq T_{m2}\\ 1 & T>T_{m2}\end{cases} \tag{12}$$

When the β is 0, the PCM is solid; When the β is 0 to 1, the PCM is the solid-liquid mixing zone; When the β is 1, the PCM is liquid.

2.2.3. Boundary conditions

In order to comply with the physical characteristics of the actual ventilation system and to ensure the stability of the flow calculation. The boundary conditions for this model are defined as follows in Table 1. The inlet type with air with a velocity of 1.8 m/s and a temperature of 35 °C is set as the speed inlet, while the outlet type is set as the pressure outlet. In order to ignore the interference of the external environment to the model. The external walls are set as adiabatic. In order to achieve multiphysics energy transfer continuity and to provide precise boundaries for the study of PCM phase transition characteristics. The interfaces between the PCP shell and the air domain, as well as between the PCM domain and the fin domain, are defined as coupling boundaries.

The temperature and heat flux on the interface between the shell and the PCM are continuous; Therefore, the coupling boundary condition are [66]:

$$T_w|_1=T_w|_2 \tag{13}$$

Table 1
Setting of boundary conditions.

Boundary	Boundary type	Temperature (°C)	Speed (m/s)
Inlet	Velocity-inlet	35	1.8
Interior	Air	-	-
	PCM	-	-
	Fin	-	-
Outlet	Pressure-outlet	-	-
Air-Wall	Adiabatic wall	-	-
PCP-Wall	Couple wall	-	-
Fin-Wall	Couple wall	-	-

$$q_w|_1 = q_w|_2 \tag{14}$$

$$-\lambda\left(\frac{\partial T}{\partial n}\right)_w|_1 = h(T_w - T_f) \tag{15}$$

The exterior air wall is insulated. Therefore, the boundary condition is [66]:

$$\left.\frac{\partial T}{\partial x}\right|_{x=0} = \left.\frac{\partial T}{\partial x}\right|_{x=l} = 0, \left.\frac{\partial T}{\partial y}\right|_{y=0} = \left.\frac{\partial T}{\partial y}\right|_{y=a} = 0, \left.\frac{\partial T}{\partial z}\right|_{z=0} = \left.\frac{\partial T}{\partial z}\right|_{z=a} = 0 \tag{16}$$

2.2.4. Material settings

Li et al. [33]. selected phase change paraffin as the PCM and stainless steel as the encapsulation material. The performance of PCM is shown in Table 2. The properties of stainless steel are shown in Table 3.

2.2.5. Calculation method

The numerical simulations were conducted using the commercial computational fluid dynamics software ANSYS Fluent. The second-order upwind scheme was employed for spatial discretization to ensure numerical accuracy. The pressure-velocity coupling was handled by the SIMPLE algorithm. The relaxation factors were maintained at their default values.

2.3. Operating condition settings

The phenomenon of melting stratification of PCP at different heights may vary. Therefore, the height of PCP was set to 500, 800, 1100, 1400 and 1700 mm to study the temperature stratification phenomenon of PCP at different heights. The fins can provide support for unmelted PCM, thereby reducing the degree of PCP thawing delamination and may even have the effect of increasing unsteady heat transfer. Therefore, the control variable method was used to study the optimization effect of different fin length (FL), number of transverse fins (NOTF) and number of longitudinal fins (NOLF) on the unsteady heat transfer performance of PCP. Depending on the size of the PCP, the fin lengths are set to 100, 200, 300, 400 and 500 mm. The fins are positioned as evenly distributed as possible and are set in the middle of the PCP. Set both NOTF and NOLF to 0, 1, 2, 3, and 4 slices. The fin thickness is 1.5 mm. Table 4 details the operating conditions.

2.4. Evaluation index

The stratification during the melting of the PCP occurs due to the natural convection driven by density differences, where solid PCM tends to remain above the liquid PCM. To quantitatively evaluate the melting uniformity, a liquid phase gradient index θ is introduced. The PCP is divided horizontally into upper and lower halves, and θ is defined as the absolute difference in liquid fraction between these two regions. The formula for this calculation is shown in 19. A smaller θ value indicates more uniform melting, while a larger θ signifies more pronounced stratification.

Similarly, to assess the temperature distribution uniformity in the air stream downstream of the PCP, a temperature inhomogeneity coefficient η is proposed. This coefficient characterizes the dispersion of the temperature field, defined as the ratio of the maximum temperature difference on a plane to the average temperature of that plane. The formula for this calculation is shown in 20. A smaller η denotes a more uniform air temperature distribution with less stratification, whereas a larger η indicates greater temperature non-uniformity.

$$\theta = f_{up} - f_{down} \tag{17}$$

Where, θ is the liquid phase component gradient; f_{up} is the liquid fraction of the upper part of the PCP; f_{down} is the liquid fraction of the lower part of the PCP.

$$\eta = \frac{(T_{max} - T_{min})}{2T_{ave}} \tag{18}$$

Table 2
Material properties.

material	Paraffin
Temperature at which melting begins (°C)	27.6
Temperature of complete thawing (°C)	29.8
Latent heat of phase change (kJ/kg)	217
Thermal conductivity (W/(m·°C))	0.21
Density (kg/m^3)	880/770
Thermal expansion coefficient (K^{-1})	5×10^{-4} (at 27.6 °C)
Viscosity (kg/m·s)	0.007
Specific heat (kJ/kg·K)	3.22

Table 3
Physical properties of packaging materials.

material	Steel
Thermal conductivity (W/(m·°C))	16
Density (kg/m^3)	8030
Specific heat (kJ/kg·K)	502

Table 4
Numerical simulation of working conditions.

Case No.	PCP height (mm)	FL (mm)	NOTF	NOLF
1	500	100	2	2
2	800	200	2	2
3	1100	300	2	2
4	1400	400	2	2
5	1700	500	2	2
6	500	100	2	2
7	500	200	2	2
8	500	300	2	2
9	500	400	2	2
10	500	500	2	2
11	500	300	0	2
12	500	300	1	2
13	500	300	2	2
14	500	300	3	2
15	500	300	4	2
16	500	300	2	0
17	500	300	2	1
18	500	300	2	2
19	500	300	2	3
20	500	300	2	4

Where, η is the temperature inhomogeneity coefficient, T_{max} is the maximum temperature of the cross-section, °C; T_{min} is the minimum temperature of cross-section, °C, T_{ave} is the average temperature of cross-section, °C.

2.5. Model validation

To validate the reliability of the numerical model, experimental data from Li et al. [33] were used for comparison. In their experiments, temperature measurements were taken at both the upper and lower sections of the PCP; however, the temperature difference between these two points at any given time was minimal. Therefore, the average temperature of the top and bottom measurement points was adopted for model validation. As illustrated in Fig. 4, the maximum error between the simulated PCP temperatures and the experimental results from Li et al. [33] is 8.02%, which remains within 10%. This discrepancy can be attributed to the presence of moisture in the air in Li et al.'s experiment, where water vapor condensation on the PCP surface impeded heat

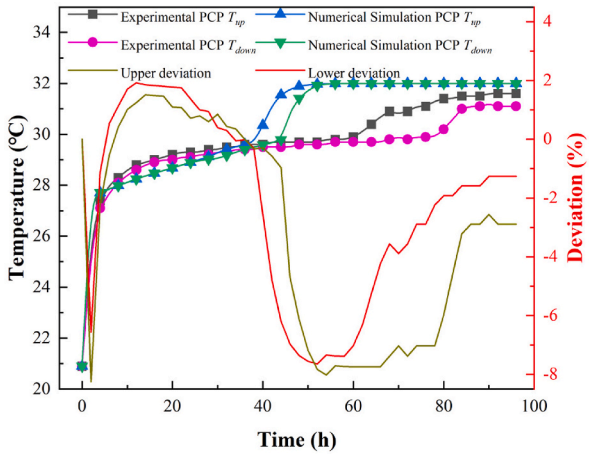

Fig. 4. Model validation.

transfer, resulting in consistently lower experimental temperatures compared to the numerical simulations. Furthermore, the numerical model successfully captured the same melting and stratification trends as those observed in the experiments. Thus, it can be concluded that the present model is reliable for investigating the stratification behavior of PCM in PCP.

3. Results and discussion

3.1. Heat transfer stratification of PCP

Fig. 5 illustrates the variation in air temperature after cooling by the PCP at different heights in the absence of fins. As shown, hot air flows from left to right and is cooled upon passing through the PCP, which simultaneously absorbs heat. At 6 h, the PCM begins to melt. At this time, the overall temperature of PCP was still low, the melting process was uniform, and the liquid fraction was distributed in the vertical direction consistently, and no significant gradient had been formed. The heat exchange between the PCP and the air was significant, and there was no obvious temperature stratification in the outlet airflow.

By 10 h, the internal melting process of the PCP is advancing. Melting and peeling began to appear. At this point, the PCM in the top region of the PCP is basically liquefied, and the liquid component in this area is larger. while in the middle and lower parts, it remains at a low level. A top-down decreasing liquid fraction distribution is formed. Due to the high temperature in this area, the heat transfer efficiency decreases. The cooling effect of the air flowing through the upper part weakens and an uneven temperature distribution begins to form. The temperature of the high liquid fraction area at the top increases high, and the heat exchange capacity is high. This is the result of a vertical gradient in the outlet air temperature.

By 14 h, most of the upper PCM has melted, the difference in the distribution of the liquid fraction in the vertical direction is further expanded, the phase transition front is clearly moved downward, the heat exchange is further weakened, and the temperature inhomogeneity of the PCP outlet air is intensified. At this time, the heat exchange mode between air and PCM is changed. The top area is dominated by the sensible heat of liquid PCM, and its heat transfer efficiency between air is low. The middle and lower parts are still dominated by latent heat absorption of phase change, and the heat transfer efficiency is relatively high. This difference in heat transfer patterns reinforces the temperature stratification of the outlet air.

By 18 h, all of the PCM in the lower region had also melted, and the liquid phase fraction throughout the PCP reached 1, indicating that all of its latent heat storage capacity had been exhausted. In the upper region of the PCP, heat exchange tends to be weak; the air flowing through the top portion is not adequately cooled, resulting in a highly non-uniform distribution of the outlet air temperature. Effective cooling mainly occurs in the lower region. At this point, the temperature stratification reaches its extreme, and the temperature profile of the outlet air directly reflects the physical reality that, after complete liquefaction, the upper region of the PCP degenerates into an inefficient sensible heat exchanger due to the lack of phase change latent heat for regulation.

This effect is particularly pronounced when the height of the PCP is 1700 mm. Over time, the temperature drop of the upper air flow gradually decreases compared to that of the lower part, and the stratification phenomenon becomes more severe as the height of the PCP increases. In essence, increasing the height amplifies the spatial scale of the non-uniform liquid phase fraction distribution, causing the gradient in heat exchange capacity resulting from this variation to become more noticeable at the outlet. Calculating the Ra, and the PCP with a height of 500 mm is 3.45×10^8 at 6 h. It was 8.37×10^{10} at 10 h, 4.14×10^{11} at 14 h, and 6.12×10^{11} at 18 h. The PCP with a height of 1700 mm is 4.50×10^{11} at 6 h. It was 1.08×10^{12} at 10 h, 5.26×10^{12} at 14 h, and 8.14×10^{12} at 18 h. The Ra number exhibits a continuous upward trend over time, indicating gradually intensified buoyancy effects and more pronounced thermal stratification inside the PCP. Moreover, the PCP with a height of 1700 mm consistently presents larger Ra values than the 500 mm-height one, demonstrating that a greater height strengthens buoyancy-driven flow and leads to a more distinct thermal stratification structure. And they are all greater than 10^3. This also corresponds to the phenomenon of temperature stratification mentioned above.

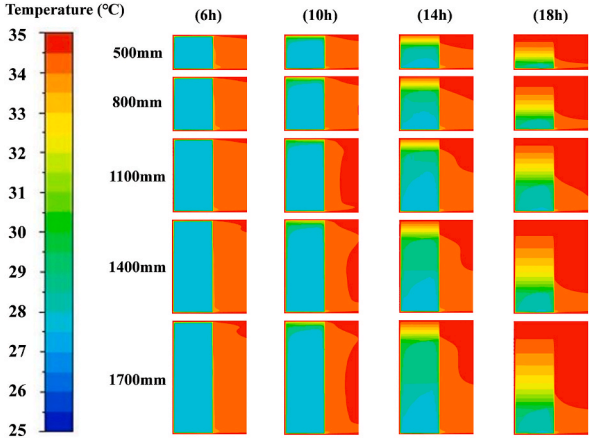

Fig. 5. Heat transfer stratification of PCP at different heights.

3.2. Melting process of the PCP

Fig. 6 depicts the temporal evolution of the average liquid fraction and temperature of PCP at different heights. As shown, both parameters generally increase over time. However, an inflection point occurs at approximately 6 h, characterized by a rapid temperature surge between 6 and 7 h and a concurrent sharp reduction in the melting rate. This phenomenon is more pronounced at greater PCP heights. Cross-referencing with the contour plots in section 3.1, this inflection is attributed to the onset of melting stratification. As the liquid PCM accumulates at the top, heat transfer in the upper region relies solely on sensible heat, which is significantly less effective than latent heat absorption. This leads to the abrupt temperature rise. Simultaneously, the reduced temperature difference between the upper liquid PCM and the lower solid PCM diminishes the heat transfer rate, slowing the melting process. Consequently, the upward trend in temperature stabilizes after 7 h as the melting rate decreases.

3.3. Sensitivity analysis

From the above analysis, it can be seen that the higher the height of the PCP, the more obvious the melting unevenness. Among them, PCP with a height of 500 mm are the least obvious. If the PCP with a height of 500 mm can change significantly after optimization, then this optimization method can also have a good optimization effect on the PCP of the remaining height. At the same time, using a PCP with a height of 500 mm can also reduce the model and reduce the calculation requirements. Therefore, in this section, a sensitivity analysis of the optimized settings is performed for a PCP with a height of 500 mm.

3.3.1. Effect of the FL

Fig. 7 shows the PCP liquid fraction over time with a PCP height of 500 mm and two FL of NOTF and NOLF. As you can see from the figure, the left part of the PCP melts faster and the right part melts more slowly. This is because the hot air moves from left to right, and the air has a higher temperature as it passes over the left part. The temperature of the air after heat exchange with the left part is low, resulting in less heat exchange with the right part, and the left side melts first, and the right side melts later. It can be seen from the figure that the PCM near the fins began to melt at 6 h, and the longer the fins, the more locations where this phenomenon occurred. At 10 h, the PCM near the fin completely melted, and the longer the fin, the greater the melting amount of PCM. At 14 h, many PCM in the upper part of the PCP had been completely thawed, and there were many unmelted PCM in the lower part. At 18 h, the PCP with no fins and 100 mm FL and 200 mm did not melt, and the rest of the NOTF were completely melted. At 6 h, the PCP began to melt and stratify a little, and a small part of the melted liquid PCM was above the PCP. At 10 h, there was a more obvious phenomenon of melting stratification, and there was more liquid PCM in the lower part at this time. The phenomenon of melt stratification was very obvious after 14 h of melting, and there were many melted PCM in the upper part of the PCP. At 14 h, the remaining solid-state PCM distribution was different for PCP with different FLs. In general, the PCP is divided into three layers by fins in the longitudinal direction, and the transverse length of each layer is different for different FL. The delamination of PCP with a FL of 100 mm is not significant, and there is very little solid-state PCM in the upper part. The PCP with a FL of 200 mm has a layering phenomenon, but because the fins are not long, it cannot effectively prevent the solid-state PCM at the transverse ends of the PCP from moving downward. There are still only a small number of solid-state PCM above the PCP. The PCP with a FL of 300 mm has obvious delamination, which can prevent some solid-state PCM at both ends of the PCP from moving downward, and a small number of solid-state PCM above the PCP. The PCP with a FL of 400 mm has obvious delamination, which can effectively prevent part of the solid-state PCM at both ends of the PCP from moving downwards and some solid-state PCM above the PCP. The PCP with a FL of 500 mm has obvious delamination, which can effectively prevent some solid-state PCM at the transverse ends of the PCP from moving downward, and there are more solid-state PCM above the PCP.

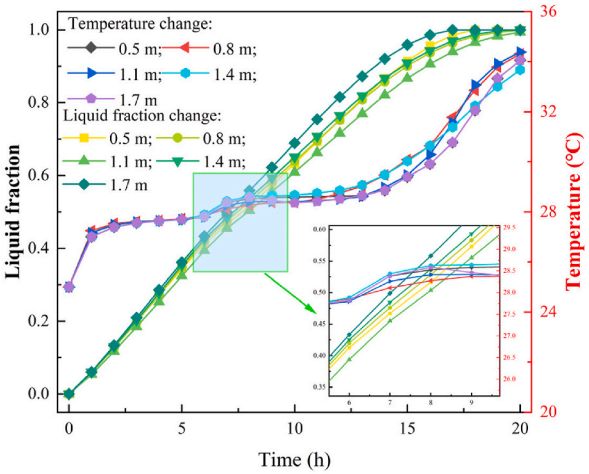

Fig. 6. Heat transfer stratification of PCP at different heights.

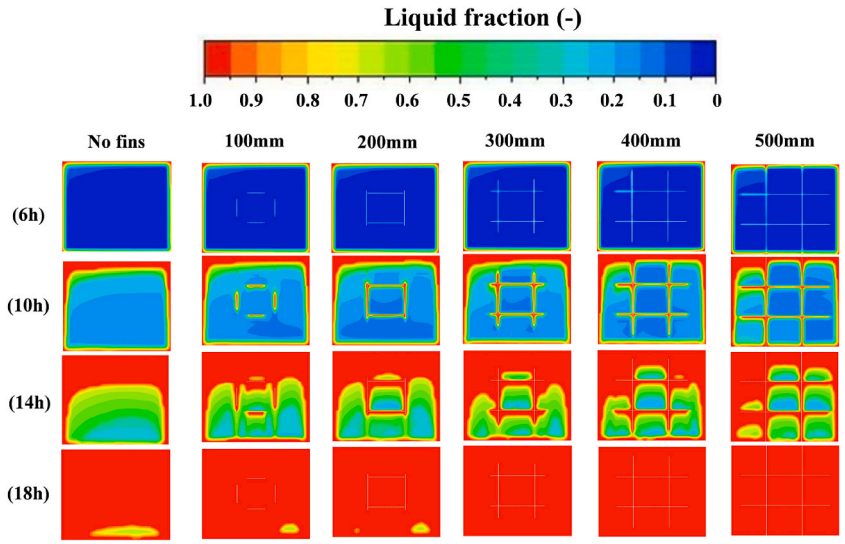

Fig. 7. Variation of PCP liquid fraction over time with different FL.

Fig. 8 illustrates the effect of FL on the optimization of unsteady heat transfer in PCP when the PCP height is 500 mm and both NOTF and NOLF are two. From Fig. 8, it can be concluded that the θ increase first rises and then decreases, because the melted liquid PCM moves to the upper part of the PCP due to gravity, which makes the liquid fraction between the upper and lower parts larger and larger. When θ reaches the maximum, there is only a small part of solid-state PCM in the upper part, and the overall melting rate in the upper part is small. There are more solid-state PCM in the upper part, and the overall melting rate in the upper part is larger. The combination of the two will make theta smaller until it melts completely. During the whole melting process, the θ of PCP with a FL of 500 mm was higher than that of PCP with a FL of 300 mm only after 14 h. But before that, it was at the lowest level. Overall, PCP with a FL of 500 mm melts more evenly. The maximum θ of FL was 0.52, 0.46, 0.38, 0.32 and 0.19 for 100 mm, 200 mm, 300 mm, 400 mm and 500 mm, respectively. The θ of PCP with finned addition was 2.93 times higher than that of PCP without finning. The results indicated that with the increase of the length of the fins, the melting stratification of PCM became less obvious. This is because the longer fins in the PCP cross-sectional direction effectively prevent the solid-state PCM at the transverse ends of the PCP from moving upwards, thus reducing theta. The addition of FL can weaken the phenomenon of PCM melting delamination.

Fig. 9 illustrates the effect of FL on the unsteady heat transfer rate of PCP. As can be seen from the figure, the fins increase the unsteady heat transfer of the PCP. Where "-" means that the liquid phase fraction has no units. PCP without fins completely melted at 18.6 h. PCP with FL of 100 mm, 200 mm, 300 mm, 400 mm, and 500 mm melted completely at 18.49 h, 18.12 h, 17.87 h, 17.01 h, and 16.58 h, respectively. The longer the fin, the shorter the melting time, and the more obvious the effect of the fin in enhancing the heat transfer rate of PCP. This is because the shell of the PCP is easily heated by the outside hot air, and the fins have strong thermal

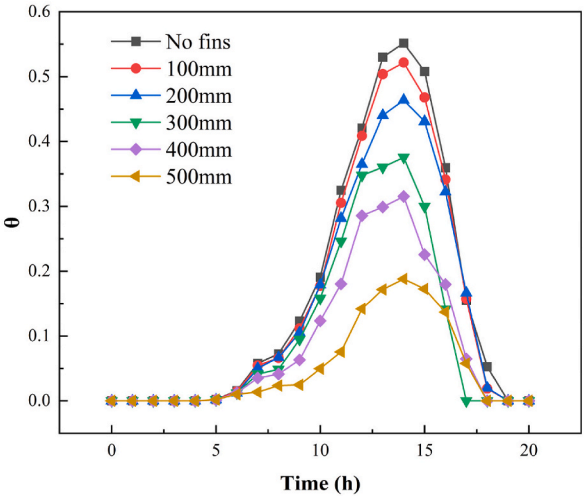

Fig. 8. Effect of FL on the optimization effect of unsteady heat transfer of PCP.

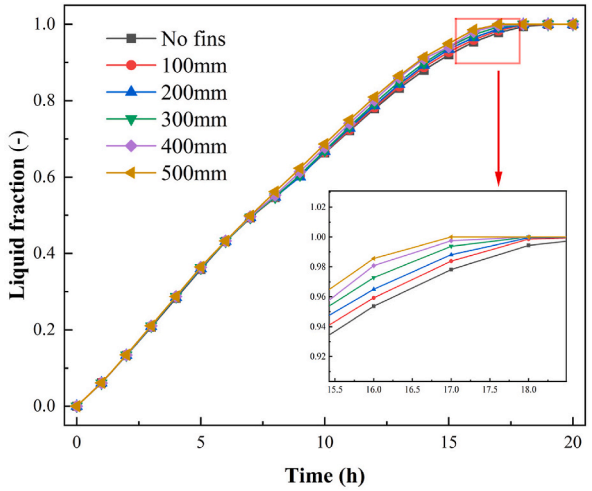

Fig. 9. Effect of FL on the unsteady heat transfer rate of the PCP.

conductivity. This causes the temperature of the fins in contact with the PCP's housing to rise more quickly. This increases the heat transfer between the PCM and the fins. FL has a great influence on the melting time of PCP. When the fin length of 100 mm was added, the complete melting time was shortened by about 0.11 h, and the heat transfer rate was only increased by about 0.59%. When the fin length of 200 mm was added, the complete melting time was shortened by about 0.48 h and the heat transfer rate was increased by about 2.58% compared with the fin. When the fins with a length of 300 mm were added, the complete melting time was shortened by about 0.73 h, and the heat transfer rate was increased by about 3.92%. When the fin length of 400 mm was added, the complete melting time was shortened by about 1.59 h, and the heat transfer rate was increased by about 8.55%. When the fins with a length of 500 mm were added, the complete melting time was shortened by about 2.02 h and the heat transfer rate was increased by about 10.86% compared with the fins without fins. The longer the fins, the more heat transfer efficiency can be increased.

3.3.2. Effect of the NOTF

Fig. 10 shows the PCP fraction of different NOTF over time at a PCP height of 500 mm, a FL of 300 mm, and a NOLF of 2 cells. As can be seen from the figure, the PCM near the fin begins to melt at 6 h, and the more NOTF, the more obvious this phenomenon becomes. At 10 h, the PCM near the fin was completely thawed, and the more NOTF, the greater the melting of PCM. At 14 h, many PCM in the upper part of the PCP had been completely thawed, and there were many unmelted PCM in the lower part. At 18 h, the PCP without fins and without transverse fins did not melt, and the rest of the NOTF were completely melted. At 6 h, the PCP began to melt and stratify a little, and a small part of the melted liquid PCM was above the PCP. At 10 h, there was already a more obvious phenomenon of melting stratification, and there were more liquid PCM in the upper part at this time. The phenomenon of melt stratification was very obvious

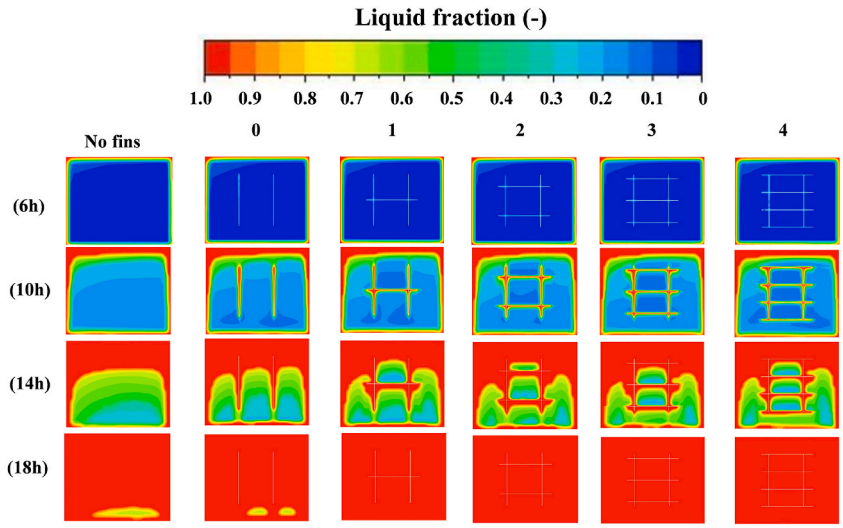

Fig. 10. Variation of PCP liquid fraction over time with different NOTF.

after 14 h of melting, and there were many melted PCM in the upper part of the PCP. At 14 h, the remaining solid-state PCM distribution was different for PCP with different NOTFs. PCP without finned versus without transverse fins are not stratified vertically, and most solid PCM are below the PCP. A PCP with a NOTF of 1 has two layers in the vertical direction, and although there are more liquid PCM in the upper part, there are still a few solid-state PCM on top of the PCP. A PCP with a NOTF of 2 has three layers in the vertical direction, and there is also a part of the solid-state PCM in the upper part of the PCP. A PCP with a NOTF of 3 has four layers in the vertical direction, but due to the small height of each layer, the top layer has completely melted, leaving only three layers. A PCP with a NOTF of 4 has five layers in the vertical direction, and as with a NOTF of 4, the top layer has completely melted due to the small height of each layer, leaving only four layers.

Fig. 11 shows the effect of NOTF on the optimization effect of PCP unsteady heat transfer when PCP height is 500 mm, FL is 300 mm, and NOLF is 2 cells. As can be seen from Fig. 11, θ decreases as NOTF increases throughout the melting process. The θ of PCP with NOTF of 4 was higher than that of NOTF 1, 2 and 3 in the first 12 h of melting, respectively. But after that, it's at the lowest level. Overall, when the NOTF is 4, the PCP melts more evenly. When the NOTF is 0, the θ variation is consistent with the absence of fins due to the absence of support in the direction of gravity. This shows that the transverse fins are important in the work of preventing uneven melting of the PCP. Even though there are many longitudinal fins, there are no transverse fins and longitudinal fins to divide the PCP into small units in the longitudinal direction. The maximum θ of NOTF 0, 1, 2, 3 and 4 were 0.54, 0.50, 0.49, 0.46 and 0.41, respectively. The results indicated that with the increase of NOTF, the melting stratification of PCM became less obvious. This is because more NOTF and NOLF will divide the PCP into more parts more evenly in the vertical direction, and the melting of one part will not affect the other part, and the effect between the parts will be smaller. The phenomenon of melting stratification is only evident in individual parts. Moreover, more NOTF prevents the unmelted solid PCM from moving towards the lower part of the PCP, thereby reducing theta. NOTF can attenuate the phenomenon of PCM melting stratification.

Fig. 12 illustrates the effect of NOTF on the unsteady heat transfer rate of PCP. As can be seen from the figure, NOTF increases the unsteady state heat transfer of PCP. PCP without fins melted completely at 18.6 h. The PCP with NOTF of 0, 1, 2, 3 and 4 completely melted at 18.32 h, 17.87 h, 17.39 h, 17.2 h and 17.01 h, respectively. The more NOTF, the shorter the melting time, and the more obvious the effect of the fins in enhancing the heat transfer rate of PCP. This is because the shell of the PCP is easily heated by the outside hot air, and the fins have strong thermal conductivity. This causes the temperature of the fins in contact with the PCP's housing to rise more quickly. Increasing the number of NOTFs can increase the contact area of the PCM with the high-temperature fins. This increases the heat transfer between the PCM and the fins. When the NOTF is 0, there are only two longitudinal fins in the PCP, and the complete melting time is shortened by about 0.3 h, and the heat transfer rate is increased by about 1.61%. When the NOTF is 1, the complete melting time is shortened by about 0.73 h, and the heat transfer rate is increased by about 3.92%. When the NOTF was 2, the melting time of PCP was shortened by about 1.21 h, and the heat transfer rate increased by about 6.51%. When the NOTF was 3, the melting time of PCP was shortened by about 1.4 h, and the heat transfer rate was increased by about 7.53%. When the NOTF was 4, the melting time of PCP was shortened by nearly 1.6 h, and the heat transfer efficiency was increased by about 8.55%. The more NOTF, the more heat transfer efficiency can be increased.

3.3.3. *Effect of the NOLF*

Fig. 13 shows the PCP fraction of different longitudinal fins with a PCP height of 500 mm, a FL of 300 mm, and a NOTF of 2 cells over time. As can be seen from the figure, the PCM near the fin begins to melt at 6 h, and the more NOLF there are, the more obvious this phenomenon becomes. At 10 h, the PCM near the fin was completely thawed, and the more NOLF, the greater the melting amount of PCM. At 14 h, many PCM in the lower part of the PCP had completely melted, and there were many unmelted PCM in the lower part. At 18 h, except for the PCP without fins, it did not melt, and the other NOLF were completely melted. At 6 h, the PCP began to melt and

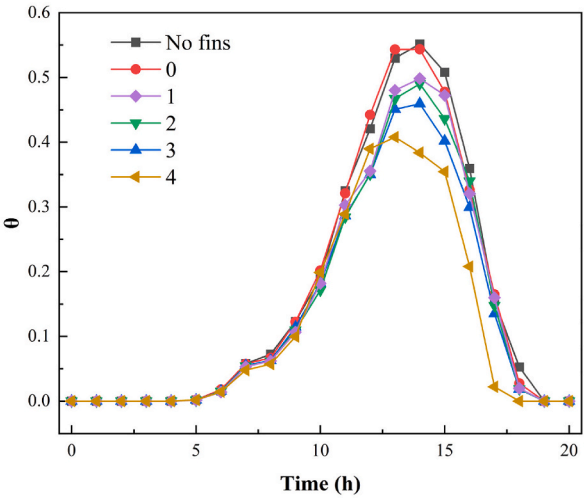

Fig. 11. Effect of NOTF on the optimization effect of unsteady heat transfer in PCP.

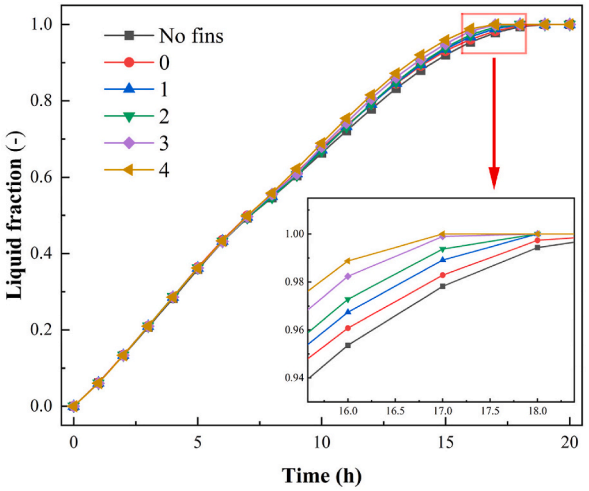

Fig. 12. Effect of NOTF on the unsteady heat transfer rate of the PCP.

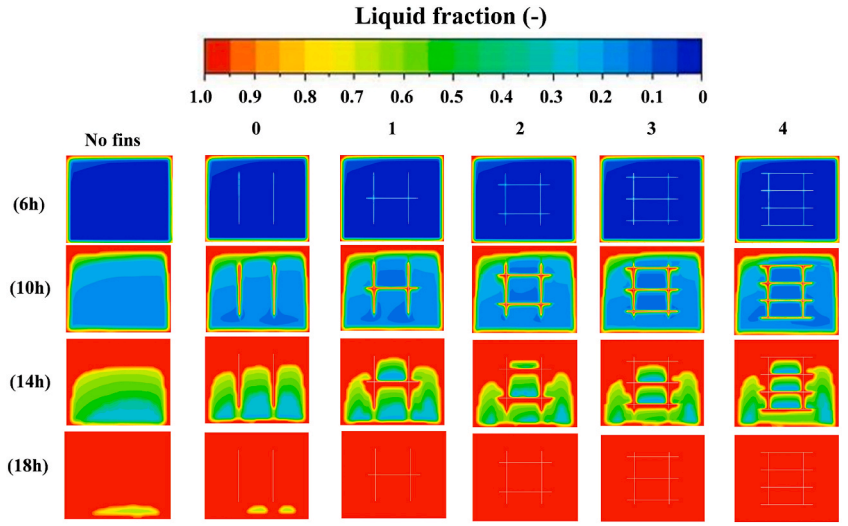

Fig. 13. Variation of PCP liquid fraction over time with different NOFL.

stratify a little, and a small part of the melted liquid PCM was above the PCP. At 10 h, there was already a more obvious phenomenon of melting stratification, and there were more liquid PCM in the upper part at this time. The phenomenon of melt stratification was very obvious after 14 h of melting, and there were many melted PCM in the upper part of the PCP. NOLF can also increase the uniformity of PCP, but its effect does not appear to be as pronounced as that of FL and NOTF.

Fig. 14 shows the effect of NOLF on the optimization effect of PCP unsteady heat transfer when the PCP height is 500 mm, the FL is 300 mm, and the NOTF is 2 cells. As can be seen from Fig. 14, θ increases as NOLF increases throughout the melting process. A PCP with a NOLF of 4 was the lowest at 11-16 h, and outside of this time, it was only lower than a PCP with a NOLF of 3. Overall, the PCP melts more evenly when the NOLF is 4. However, when the NOLF is 0, there is no significant difference between θ when the NOLF is 0 and the PCP without fins because it has two transverse fins. This again illustrates the importance of transverse fins in the work of preventing uneven melting of PCP. It prevents the unmelted solid-state PCM from moving towards the lower part of the PCP due to gravity. The maximum θ of NOLF of 0, 1, 2, 3 and 4 were approximately 0.51, 0.50, 0.49, 0.46 and 0.44, respectively. The results indicated that with the increase of NOLF, the melting stratification phenomenon of PCM was less obvious, but the increase of inhomogeneity was smaller. This is because even though there are many longitudinal fins, the NOTF is certain and cannot form more small parts in the vertical direction that do not affect each other. However, during the melting process, when the solid-state PCM moves downward, the lower part of the PCP has more solid-state PCM and the lower part melts faster, while the upper part has less solid-state PCM and the upper part melts at a slower rate, which will make theta decrease. As the NOLF increases, the larger the heat transfer rate, the greater the difference between the melting rate of the upper part and the lower part, and the θ will be smaller.

Fig. 15 illustrates the effect of NOLF on the unsteady heat transfer rate of PCP. As can be seen from the figure, NOLF increases the

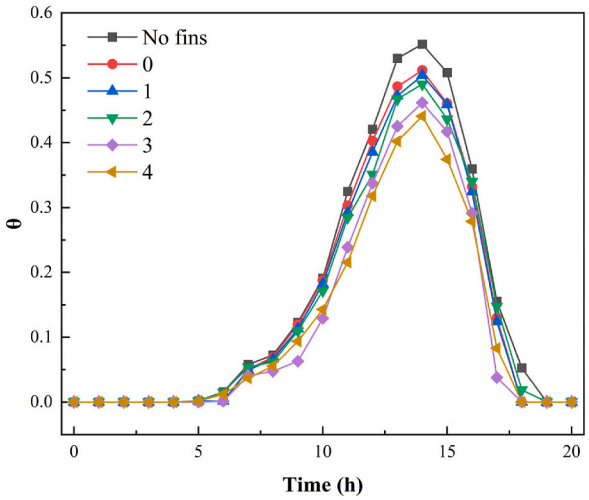

Fig. 14. Effect of the NOLF on the optimization effect of unsteady heat transfer in PCP.

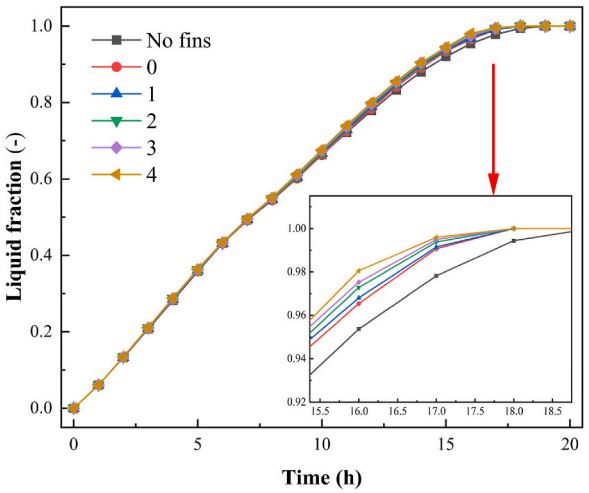

Fig. 15. Effect of the NOLF on the unsteady heat transfer rate of the PCP.

unsteady state heat transfer of PCP. PCP without fins melted completely at 18.6 h. The PCP with NOLF of 0, 1, 2, 3 and 4 melted completely at 17.9 h, 17.73 h, 17.39 h, 17.1 h and 16.91 h, respectively. The more NOLF, the shorter the melting time, and the more obvious the effect of the fin in enhancing the heat transfer rate of PCP. Moreover, this melting time is lower than that of PCP corresponding to NOTF. This is because during the melting process, there is more solid-state PCM in the upper part, and increasing the NOF will increase the contact area between the upper part of the PCP with more solid-state PCM and the high-temperature fins. However, when the transverse fins are added, the height of the fins is not high enough, and when many solid-state PCM are completely melted to the point that the remaining solid-state PCM exceed the transverse fins, the transverse fins have little effect on the melting of PCP. The longitudinal fins, on the other hand, have more time to contact with the solid PCM during the entire melting process. This causes the temperature of the fins in contact with the PCP's housing to rise more quickly. Increasing the number of NOTF can increase the contact area of the PCM with the high-temperature fins. This increases the heat transfer between the PCM and the fins. When the NOLF is 0, there are only two transverse fins in the PCP, and the complete melting time is shortened by about 0.7 h and the heat transfer rate is increased by about 3.76% compared with the non-finned fins. When the NOTF is 1, the complete melting time is shortened by about 0.87 h, and the heat transfer rate is increased by about 4.68%. When the NOTF was 2, the melting time of PCP was shortened by about 1.21 h, and the heat transfer rate increased by about 6.51%. When the NOTF was 3, the melting time of PCP was shortened by about 1.5 h, and the heat transfer rate was increased by 8.06%. When the NOTF was 4, the melting time of PCP was shortened by nearly 1.69 h, and the heat transfer efficiency was increased by about 9.09%. The more NOLF, the more heat transfer efficiency can be increased.

3.4. PCP heat transfer optimization settings

In order to compare the effect of the optimized PCP, the PCP with obvious stratification phenomenon was selected to have an effect. A PCP with a height of 1.70 m was selected for the optimization effect test. From the previous analysis, it can be seen that to solve the phenomenon of PCP temperature stratification, the best way is to divide PCP into more units that do not affect each other in the longitudinal direction. Considering that when the height of the individual element is low, the longitudinal fins may have less effect on theta. Therefore, in this section, two optimizations are adopted, the first is to divide the height of 1700 mm into 17 longitudinal units, each with a height of 100 mm. Transversely divided into 5 units, each 125 mm wide. The second optimization is to divide the height of 1700 mm longitudinally into 17 units, each with a height of 100 mm. Do not add any fins in the transverse direction.

3.5. PCP heat transfer optimization results

3.5.1. Contour differences

Fig. 16 shows the optimized results of a PCP of 1700 mm. As can be seen from the figure, the optimized PCP will be very uniform in both optimization methods. At 6 h, the two optimization methods were not much different from those without optimization. At 10 h, a more obvious high temperature region began to appear on the left side of the PCP of optimized mode 1. At 14 h, there is a more obvious high temperature zone on the left side of optimization method 1. At 18 h, all three modes of PCP lost their cooling ability. However, in this case, the left part of the PCP in Optimization Method 1 has a larger high temperature area, and the right side will have a lower temperature than in Optimization Method 2. This is due to the longitudinal fins in Optimization Method 1, which increase heat transfer. After optimizing the left side of method 1, the air transfers more heat between the PCP and the air temperature, and the air temperature will be lower. Air with a lower temperature reduces heat transfer as it passes over the right side of the PCP. This makes the PCP temperature more unevenly distributed between the left and right.

Fig. 17 shows the velocity distribution and velocity vector before and after optimization due to natural convection within the PCP. The flow rate of unoptimized PCP was the highest, especially at 8×10^{-4} m/s in the later stage. Indicates the presence of strong natural convection, which is the direct cause of thermal stratification. The flow rate of optimization method 1 is the lowest in each period, and it moves within the respective units. The flow rate of optimization method 2 is also low at all times. However, it is faster than optimization method 1. This confirms that the fins are effectively segmented and weakens large-scale convective circulation. This is reconstituted into a more uniform weak flow, thus addressing the phenomenon of temperature stratification. The fins not only enhance heat transfer, but also inhibit the original natural convection. This weakening of natural convection results in a limited increase in the overall heat transfer rate.

3.5.2. η difference

The η at 0.2 m after PCP was calculated and the uniformity of the air after PCP was compared between the two optimization methods. The results are shown in Fig. 18, and it can be seen that all the methods have a high temperature when passing through the bottom and top of the PCP due to the weak heat transfer between the bottom and top of the PCP and the air. When the air temperature after passing through PCP is low, there will be a large error in the η. Therefore, we will remove this part of the data. The calculation results are shown in Fig. 18. As can be seen from the figure, the η of the two optimization methods is smaller than before optimization. This shows that two optimization methods can effectively reduce the temperature inhomogeneity. Compared with the PCP without optimization, the η of the optimized by optimization method 1 can be reduced by 0.316 on average. Optimization method 2 can reduce the η by an average of 0.233 in this process. Moreover, optimization method 1 is only smaller than optimization method 2 after 18 h. This shows that optimization method 1 can be more effective in reducing the temperature inhomogeneity.

3.5.3. Differences in the melting process

Fig. 19 shows the melting process of a PCP with a height of 1700 mm under two optimizations. The non-optimized PCP showed abrupt changes in liquid fraction and temperature between 6 and 7 h. The PCP of Optimization Method 2 also had a mutation at the same time, but the amount of mutation was small. The PCP of Optimization Method 1 remains unchanged at the same time. The cause of the mutation is the movement of liquid PCM to the upper part of the PCP. This shows that optimization method 1 can better prevent the occurrence of melting delamination.

3.5.4. Differences in liquid fraction distributions

Fig. 20 shows the heat transfer optimization results of the two optimization methods. Fig. 20 (a) shows the liquid fraction at different heights of 1700 mm PCP for two optimizations. As can be seen from the figure, the liquid phase fraction of the two optimization methods is uniform in the height range of 0.2-1.6 m, and the liquid phase fraction is higher at 0-0.1 m and 1.6-1.7 m. This is because one of the two height ranges of PCM in contact with the PCP housing is in direct contact with the air, which increases their melting rate. In addition, the liquid fraction of Optimization Method 1 is higher than that of Optimization Method 2. This is because Optimization Method 1 will have more fins in contact with the PCM, which will increase the melting rate of Optimization Method 1 during the mid-thaw period. However, at 14 h, the difference between the two optimization methods is not large. Fig. 20 (b) shows the changes in Nu under three different optimization methods are shown. The optimization strategy effectively improves and stabilizes the heat transfer performance, and the optimization method 1 maintains the highest and most stable Nu value throughout the entire test process. This is the same conclusion as above.

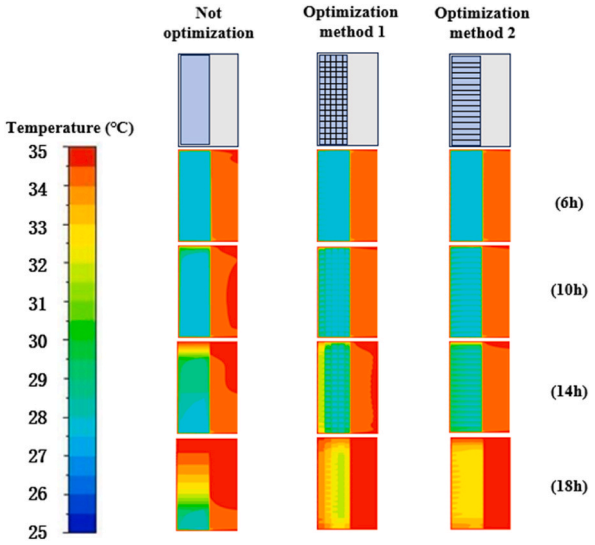

Fig. 16. Overall temperature contour before and after optimization.

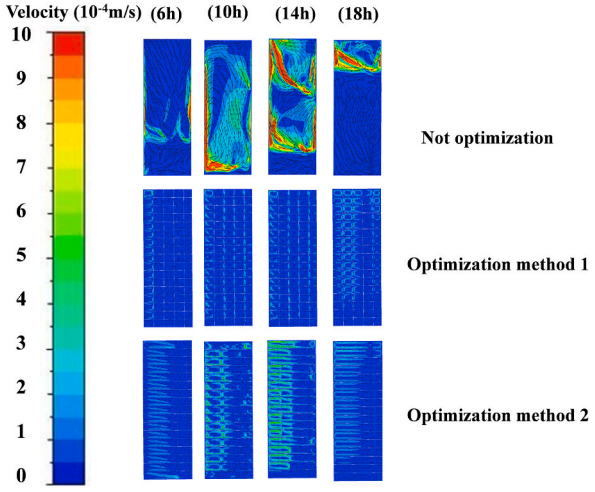

Fig. 17. PCP internal velocity contour before and after optimization.

3.6. PCP optimization suggestions

3.6.1. Thermodynamic benefit analysis

Since the inlet conditions are the same, the inlet air input is in the same state for both methods. The thermodynamic indicators of the two systems are calculated based on the final state in Fig. 19 of the thermal properties of the PCM. The calculation results are shown in Table 5. Although the average final temperature and total heat absorption of method 2 are slightly higher due to temperature stratification, the entropy increases greater, indicating stronger internal irreversibility. As a result, the storage capacity of option 1 is about 1.9% higher. This proves that method 1 reduces irreversible losses in the heat transfer process by promoting uniform melting, and more effectively preserves the "quality" of the input energy. From the perspective of the second law of thermodynamics, option 1 is a better choice.

3.6.2. Cost analysis

In order to deeply evaluate the engineering application value of fin structure optimization, the cost-benefit analysis of the two methods is carried out as shown in Table 6. Method 1: A total of 2 pieces of stainless steel with a length of 1700 mm and a width of 600 mm, a length of 1700 mm and a width of 60 mm, a length of 600 mm and a width of 60 mm, 16 pieces of 600 mm and a width of 60 mm and 4 pieces of stainless steel with a length of 1700 mm and a width of 60 mm were used. A total of 3.3 m^2 of stainless steel is required. Method 2: A total of 2 pieces of stainless steel with a length of 1700 mm and a width of 600 mm, a length of 1700 mm and a width of 60

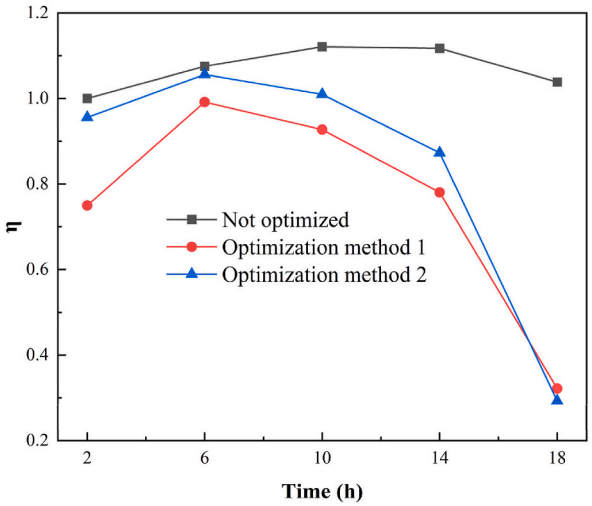

Fig. 18. Temperature inhomogeneity coefficient before and after optimization.

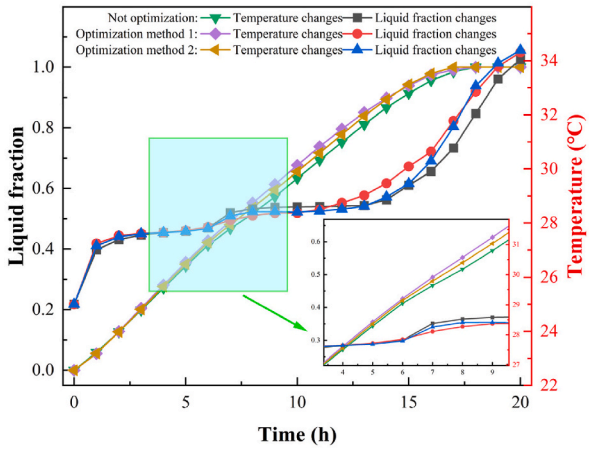

Fig. 19. The two optimization methods are different heights of the liquid phase fraction.

mm, a length of 600 mm and a width of 60 mm, and 16 pieces of stainless steel with a length of 600 mm and a width of 60 mm were used. A total of 2.892 m^2 of stainless steel is required. Market research shows that the unit price of stainless steel materials with a thickness of 1.5 mm is about 28.6 $/$m^2$, and the unit price of processing is about 15 $/$m^2$. Method 1 costs about $143.88, and method 2 costs about $126.09. Compared to method 2, the cost of the board for method 1 is increased by $17.79. Fig. 18 shows that the melting time of method 1 compared with method 2 can be shortened by 5.2%. Fig. 17 shows that the uniformity of method 1 compared with method 2 can be improved by 26.3%. Quantitative calculations show that for every $1 of additional cost investment, about 0.29% melting time savings and 1.48% uniformity improvement can be obtained. This trade-off indicates that although method 1 is more costly, its benefits in improving melting efficiency and temperature uniformity are more prominent. It is especially suitable for scenarios where the reliability of thermal management is critical, such as data centers. Method 2 is suitable for scenarios with relatively small requirements for thermal management reliability (such as underground refuge chambers, building energy storage).

3.7. Comparison of existing studies

This study focuses on the melting uniformity of PCM in heat storage and thermal management applications, and compares the existing optimization methods. Due to the different sizes of phase change thermal storage devices in different studies. Therefore, the cost of the equipment in different studies is compared with the volume price of PCM to obtain the cost per unit volume of PCM. The comparison results are shown in Table 7. Li et al. [55], although the application of fractal fins in the photovoltaic-phase change system observed the mitigation of melting and delamination. However, the research focuses on the temperature uniformity of photovoltaic panels, and does not deeply reveal and optimize the physical mechanism of melting and stratification within PCM. Tu et al. [56] enhanced the melting uniformity of PCM by introducing array heat exchanger tubes, but this method significantly increased the

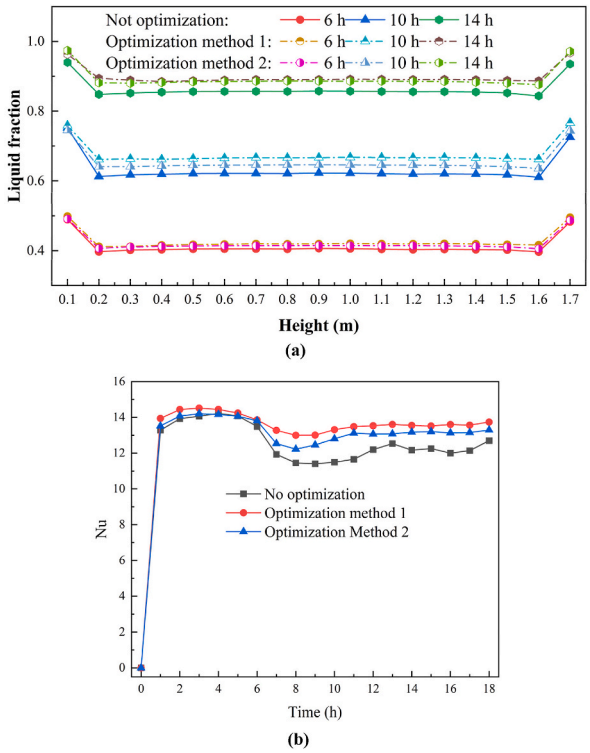

Fig. 20. Heat transfer optimization results of two optimization methods: (a) Liquid fraction at different heights; (b)Nu.

Table 5
Cost comparison of the two optimization methods.

Index	Optimization method 1	Optimization method 2
Final average temperature (°C)	34.67	34.84
The internal energy increases. (kJ/kg)	248.12	248.68
Entropy increase (kJ/kg·K)	0.8215	0.8234
Storing exergy (kJ/kg)	3.23	3.17

Table 6
Cost comparison of the two optimization methods.

Optimization method	Material area (m^2)	Unit price of materials ($/$m^2$)	Pocessing unit price ($/$m^2$)	total unit price ($/$m^2$)	Cost ($)
1	3.3	28.6	15	43.6	143.88
2	2.892				126.09

Table 7
Comparison of existing studies.

Related research	Method	structural complexity	Cost($/L)	Improvement in effectiveness
Li et al. [55]	bifurcated fractal fins	Complex	9.54	Stratified response observed, no quantitative analysis performed
Tu et al. [56]	Array heat exchange tubes	Complex	23.86	Homogeneity improvement, unspecified percentage
Xu et al. [57]	PCP structure optimization	Simple	3.39	93%
This Work	Fin arrangement	simple	2.06	293%

complexity and cost of the system. Xu et al. [57] achieved a 93% improvement in melting uniformity through structural optimization, highlighting the key impact of structural design. However, this study does not specifically focus on the specific physical scenario of melting stratification dominated by strong natural convection in PCP. In contrast, the fin configuration optimization strategy proposed in this study not only improves the performance by 293% with simple structure and low cost. More importantly, it significantly improves uniformity while maintaining the economics and engineering practicability of the system.

4. Conclusion

This study revealed the mechanism of delamination during PCP melting. This phenomenon significantly reduces heat transfer efficiency, triggers local overheating, and can lead to phase change failure. In order to effectively suppress this phenomenon, an optimized method for introducing a fin structure into PCP was proposed and verified. In this study, the inhibition effect of key parameters such as FL, NOTF and NOLF on the melting stratification phenomenon and their comprehensive effect on the overall melting rate of PCP were systematically explored. The results can be used in building energy storage, underground refuge chambers, and data centers. The main conclusions are as follows.

(1) The formation of the molten layer is closely related to the height of the plate, and its degree increases significantly with increasing height. Among the various structures studied, the structure with a plate height of 1700 mm exhibited the most obvious thermal stratification. This is particularly challenging for those high-height, plate-like phase change storage devices. Because proactive measures must be taken to ensure uniformity in heat distribution.
(2) There is a key engineering balance issue in the design of the PCP: while extending the FL to 500 mm does significantly improve temperature uniformity (reducing maximum θ by 64%), the resulting heat transfer efficiency improvement is limited (only about 10.86%). This finding suggests that in order to improve the stability and reliability of the system, it is entirely possible to improve the temperature uniformity without affecting the melting rate. This is an important reference for systems that are designed with uniform heat distribution as the goal rather than maximum power density.
(3) In application scenarios where high requirements are placed on temperature uniformity and the quality of energy, although method 1 increases the cost of the individual material components by approximately 83%, it nonetheless achieves a 26.3% improvement in uniformity and a 1.9% increase in energy efficiency. The additional investment required through this solution effectively helps to mitigate system risks associated with local overheating. Method 2, on the other hand, enables the basic phase transition functionality at a lower initial cost, making it a more economical and viable option.

The application potential of the optimization method based on this study in practical scenarios. Future research should focus on the development and verification of engineering prototypes for building energy storage walls, underground refuge chambers, and data center cabinet cooling systems. Focus on evaluating its thermal performance under different operating conditions, integration feasibility with existing systems, and cost-effectiveness throughout its life cycle. To promote the application of phase change heat storage technology in specific industrial scenarios.

CRediT authorship contribution statement

Shiyu Liao: Writing – review & editing, Writing – original draft, Software, Data curation, Conceptualization. **Xiang Li:** Writing – review & editing, Software, Data curation. **Jiri Zhou:** Methodology, Data curation, Conceptualization. **Xiaoyan Yi:** Writing – review & editing, Data curation. **Ruiyong Mao:** Methodology, Data curation. **Hongwei Wu:** Methodology, Data curation. **Zujing Zhang:** Writing – review & editing, Methodology.

Declaration of competing interest

We declare that we have no financial and personal relationships with other people or organizations that can inappropriately influence our work, there is no professional or other personal interest of any nature or kind in any product, service and/or company that could be construed as influencing the position presented in, or the review of, the manuscript entitled ***'Numerical study on unsteady heat transfer characteristics of phase change plates optimized by fin structure'***.

Acknowledgments

The authors would like to thank the financial support from the Natural Science Foundation of Guizhou Province (No. ZD [2026] 040), the National Natural Science Foundation of China (NO. 52168013), the Laboratory of Guizhou University Open Fund Project (No.SYSKF2025-024), the Guizhou Province Postgraduate Research Fund Project (NO.2024YJSKYJJ114),the Innovation and Entrepreneurship Training Program for College Students of Guizhou University Project (NO.gzusc2025130), and the SRT Program Project of Guizhou University (NO.2025SRT528).

Data availability

Data will be made available on request.

References

[1] C. Yupanqui, N. Dias, M.R. Goodarzi, S. Sharma, H. Vagheei, R. Mohtar, A review of water-energy-food nexus frameworks, models, challenges and future opportunities to create an integrated, national security-based development index, Energy Nexus 18 (2025) 100409, https://doi.org/10.1016/j.nexus.2025.100409.

[2] L. Wu, C. Xu, Q. Zhu, D. Zhou, Multiple energy price distortions and improvement of potential energy consumption structure in the energy transition, Appl. Energy 362 (2024) 122992, https://doi.org/10.1016/j.apenergy.2024.122992.

[3] X. Dai, X. Xu, Bump in energy prices and their impact on natural resources: energy transition initiatives in OECD countries, Resour. Policy 87 (2023) 104244, https://doi.org/10.1016/j.resourpol.2023.104244.

[4] Y. Yan, Z. Liu, L. Zeng, W. Li, H. Yang, H. Gao, Evaluation of the heat transfer and energy efficiency of a solar phase change heat storage system with a novel heat transfer structure, Energy Convers. Manag. 340 (2025) 120000, https://doi.org/10.1016/j.enconman.2025.120000.

[5] Q. Yang, H. Yao, Y. Yang, M. Azaiez, Effect of contact thermal resistance and skeleton thermodynamic properties on solid-liquid phase change heat transfer in porous media: a simulation study, Energy 300 (2024) 131532, https://doi.org/10.1016/j.energy.2024.131532.

[6] V.C. Midhun, M. Maroliya, S.K. Saha, Numerical investigation and optimisation of solid–solid phase change material composite-based plate-fin heat sink for thermal management of electronic package, Appl. Therm. Eng. 248 (2024) 123183, https://doi.org/10.1016/j.applthermaleng.2024.123183.

[7] Z. Zhang, Y. Wang, I.S.M. Jimidar, X. Ye, Solid–liquid–gas-like phase transition in electric field driven dense granular media, Int. J. Multiphas. Flow 179 (2024) 104907, https://doi.org/10.1016/j.ijmultiphaseflow.2024.104907.

[8] K. Zeng, Q. Zhang, C. Sheng, B. Chi, H. Zuo, H. Yang, H. Chen, Optimized study of continuous latent and sensible heat storage with multi-energy composition based on energy and power characteristics, Appl. Therm. Eng. 273 (2025) 126406, https://doi.org/10.1016/j.applthermaleng.2025.126406.

[9] J. Morales-Rodríguez, Y. Peña-Méndez, I. Gómez, S.A. Gamboa, M.F. Retana-Betancourt, Facile synthesis of the Bi2S3@rGO composite via chemical precipitation for potential applications in electrochemical energy storage, J. Energy Storage 125 (2025) 116948, https://doi.org/10.1016/j.est.2025.116948.

[10] X. Li, Z. Zhang, J. Zhou, R. Mao, H. Wu, X. Liang, Numerical and experimental study on the influence of thermal behavior of phase change plate in high temperature and low ventilation speed environment, J. Energy Storage 115 (2025) 115977, https://doi.org/10.1016/j.est.2025.115977.

[11] T. Lu, Y. Liu, B. Xin, H. Zhou, W. Xia, Dual-temperature responsive phase change waterborne polyurethane composite material suitable for personal thermal management and solar energy storage, J. Energy Storage 135 (2025) 118377, https://doi.org/10.1016/j.est.2025.118377.

[12] P.K.S. Rathore, B.S. Sikarwar, Thermal energy storage using phase change material for solar thermal technologies: a sustainable and efficient approach, Sol. Energy Mater. Sol. Cell. 277 (2024) 113134, https://doi.org/10.1016/j.solmat.2024.113134.

[13] M. Asghari, S. Fereidoni, L. Fereidooni, M. Nabisi, A. Kasaeian, Energy efficiency analysis of applying phase change materials and thermal insulation layers in a building, Energy Build. 312 (2024) 114211, https://doi.org/10.1016/j.enbuild.2024.114211.

[14] K. Li, L. Shi, Y. Zhang, Y. Yao, C. Zhang, H. Tian, G. Shu, Study on electric vehicle thermal management system using phase change materials and CO2 heat pump waste heat recovery under cold conditions, Appl. Therm. Eng. 252 (2024) 123669, https://doi.org/10.1016/j.applthermaleng.2024.123669.

[15] Y. Xie, J. Liu, W. Ma, J. Sheng, P. Zhang, Review of the heat transfer enhancement for phase change heat storage devices, J. Energy Storage 86 (2024) 111336, https://doi.org/10.1016/j.est.2024.111336.

[16] Z. Fan, L. Jiang, Y. Zhao, Y. Gao, X. Bai, S. Dong, Integrating interlayer ventilation into phase change walls: comprehensive performance and optimization in summer, Energy 307 (2024) 132741, https://doi.org/10.1016/j.energy.2024.132741.

[17] L. Jiang, Y. Gao, C. Zhuang, C. Feng, X. Zhang, J. Guan, Experiment verification and simulation optimization of phase change material cool roof in summer – A case study of Chongqing, China, Energy 293 (2024) 130613, https://doi.org/10.1016/j.energy.2024.130613.

[18] D. Seo, S.-G. Jeong, Dynamic heat transfer and electric energy consumption performance of dry floor heating systems mixed with low-cost phase-change material and activated carbon for field application, Energy Build. 337 (2025) 115694, https://doi.org/10.1016/j.enbuild.2025.115694.

[19] Z. Fan, L. Jiang, Y. Zhao, Y. Gao, X. Bai, S. Dong, Experimental and numerical study of a novel interlayer ventilation phase change wall: energy storage parameters and annual load characteristics, Energy Build. 324 (2024) 114906, https://doi.org/10.1016/j.enbuild.2024.114906.

[20] C. Zhang, R. Yang, Y. Lu, M. Arıcı, Y. Ma, X. Yang, Z. Qi, D. Li, Parametric research on thermal and optical properties of solid-solid phase change material packaged in glazing windows, J. Energy Storage 83 (2024) 110562, https://doi.org/10.1016/j.est.2024.110562.

[21] X. Zuo, Q. Li, Y. Tang, Y. Li, X. Zhao, H. Yang, Experimental and numerical investigation of building envelopes constructed with mineral based composite phase change material for thermal management, Constr. Build. Mater. 474 (2025) 141067, https://doi.org/10.1016/j.conbuildmat.2025.141067.

[22] W. Li, F. Wang, W. Cheng, X. Chen, Q. Zhao, Study of using enhanced heat-transfer flexible phase change material film in thermal management of compact electronic device, Energy Convers. Manag. 210 (2020) 112680, https://doi.org/10.1016/j.enconman.2020.112680.

[23] F. Yi, J. E, B. Zhang, H. Zuo, K. Wei, J. Chen, H. Zhu, H. Zhu, Y. Deng, Effects analysis on heat dissipation characteristics of lithium-ion battery thermal management system under the synergism of phase change material and liquid cooling method, Renew. Energy 181 (2022) 472–489, https://doi.org/10.1016/j.renene.2021.09.073.

[24] X. Ma, Q. Zhang, S. Zou, An experimental and numerical study on the thermal performance of a loop thermosyphon integrated with latent thermal energy storage for emergency cooling in a data center, Energy 253 (2022) 123946, https://doi.org/10.1016/j.energy.2022.123946.

[25] X. Wu, W. Li, Y. Wang, Z. Chang, C. Wang, C. Ding, Experimental investigation of the performance of cool storage shelf for vertical open refrigerated display cabinet, Int. J. Heat Mass Tran. 110 (2017) 789–795, https://doi.org/10.1016/j.ijheatmasstransfer.2017.03.071.

[26] D. Mađerić, B. Pavković, K. Lenić, An experimental research on energy efficiency of a beverage cooler with the latent heat storage, Appl. Therm. Eng. 148 (2019) 270–277, https://doi.org/10.1016/j.applthermaleng.2018.11.026.

[27] T. Korth, F. Loistl, A. Storch, R. Schex, A. Krönauer, C. Schweigler, Capacity enhancement of air conditioning systems by direct integration of a latent heat storage unit, Appl. Therm. Eng. 167 (2020) 114727, https://doi.org/10.1016/j.applthermaleng.2019.114727.

[28] A.A.M. Omara, A.A.M. Mohammedali, R. Dhivagar, Helmets cooling with phase change materials: a systematic review, J. Energy Storage 72 (2023) 108555, https://doi.org/10.1016/j.est.2023.108555.

[29] H. Liu, F. Zhou, X. Shi, K. Sun, Y. Kou, P. Das, Y. Li, X. Zhang, S. Mateti, Y. Chen, Z.-S. Wu, Q. Shi, A thermoregulatory flexible phase change nonwoven for all-season high-efficiency wearable thermal management, Nano-Micro Lett. 15 (2023) 29, https://doi.org/10.1007/s40820-022-00991-6.

[30] B. Liu, H. Wang, G. Zhang, J. Li, Experimental study on improvement effect of a cooling vest on thermal comfort of manufactory workers, J. Build. Eng. 68 (2023) 106067, https://doi.org/10.1016/j.jobe.2023.106067.

[31] Y. Jing, Z. Zhao, X. Cao, Q. Sun, Y. Yuan, T. Li, Ultraflexible, cost-effective and scalable polymer-based phase change composites via chemical cross-linking for wearable thermal management, Nat. Commun. 14 (2023) 8060, https://doi.org/10.1038/s41467-023-43772-4.

[32] Y. Yang, Y. Xia, F. Chen, Y. Zhu, F. Xu, L. Sun, K.S. Novoselov, P. Huang, H. Pan, H. Lin, H. Hu, L. Song, Y. Gao, D. Cai, Z. Cao, J. Zeng, Hexagonal boron nitride-induced lamellar-structured flexible phase change film for temperature-controlled information storage and wearable thermal regulation, J. Energy Storage 72 (2023) 108443, https://doi.org/10.1016/j.est.2023.108443.

[33] X. Li, Z. Zhang, R. Mao, X. Liang, J. Zhou, H. Wu, Experimental investigation on thermal performance of phase change plates used in hot and humid environment with ventilation, J. Build. Eng. 104 (2025) 112420, https://doi.org/10.1016/j.jobe.2025.112420.

[34] X. Gao, Y. Xiao, p. Gao, Z. Zhang, M. Sun, Experimental study of the effect of high humidity on the phase change plate thermal storage under natural convection, Energy 256 (2022) 124645, https://doi.org/10.1016/j.energy.2022.124645.

[35] M.A. Said, H.S. Sultan Aljibori, J.M. Mahdi, H.I. Mohammed, P. Talebizadehsardari, A. Keshmiri, Modifying the performance kinetics in the shell-and-multi tube latent heat storage system via dedicated finned tubes for building applications, J. Build. Eng. 97 (2024) 110722, https://doi.org/10.1016/j.jobe.2024.110722.

[36] Y. Hong, Y. Shi, D. Bai, F. Jiao, J. Du, Numerical study of phase change material partitioned cavities coupled with fins for thermal management of photovoltaic cells, Case Stud. Therm. Eng. 56 (2024) 104200, https://doi.org/10.1016/j.csite.2024.104200.

[37] C. Wang, P. Liu, K. Liu, S. Su, X. Cheng, Z. Wang, Study of the effect of layered structure on phase separation and heat transfer properties of phase change materials, J. Energy Storage 84 (2024) 110705, https://doi.org/10.1016/j.est.2024.110705.

[38] J.M. Mahdi, A.M. Abed, H.A. Al-Saaidi, N. Ben Khedher, R.K. Ibrahim, M. Ben Amara, Augmenting the thermal response of helical coil latent-heat storage systems with a central return tube configuration, Case Stud. Therm. Eng. 51 (2023) 103607, https://doi.org/10.1016/j.csite.2023.103607.

[39] H.E. Abdellatif, A. Belaadi, A. Arshad, H. Alshahrani, S.A. Khan, H. Mukalazi, D. Ghernaout, Enhancement of phase change material-based thermal energy storage system through container geometries: a numerical analysis, Appl. Therm. Eng. 279 (2025) 128029, https://doi.org/10.1016/j.applthermaleng.2025.128029.

[40] H. Waqas, M. Hussain, S. Khalid, Q.M. Al-Mdallal, T. Muhammad, Investigation of the impact of triangular shape fins to enhancing the melting rate of phase change materials in triplex tube heat exchanger, Int. Commun. Heat Mass Tran. 162 (2025) 108601, https://doi.org/10.1016/j.icheatmasstransfer.2025.108601.
[41] M. Danışmaz, Geometric analysis of pin fin heat sinks: effects of ellipticity and perforation for fin on heat transfer, Case Stud. Therm. Eng. 74 (2025) 106918, https://doi.org/10.1016/j.csite.2025.106918.
[42] A. Jaberi, S. Hossainpour, Enhanced PCM melting performance in shell and tube latent heat thermal energy storage systems using optimally positioned porous fins, Case Stud. Therm. Eng. 73 (2025) 106731, https://doi.org/10.1016/j.csite.2025.106731.
[43] J.R. Bhowmik, M.S. Mia, H.M.T.A. Zisan, Embedding lower fin to enhance the thermal performance of phase-change material, Therm. Sci. Eng. Prog. 66 (2025) 104009, https://doi.org/10.1016/j.tsep.2025.104009.
[44] J. Zou, W. Ge, J. Li, H. Fukuda, X. Meng, Experimental investigation of heat transfer in copper foam and solid copper fin for spherical encapsulated phase-change material based on equal filling ratio, Int. Commun. Heat Mass Tran. 168 (2025) 109495, https://doi.org/10.1016/j.icheatmasstransfer.2025.109495.
[45] W. Guo, Z. Zhang, X. Liang, H. Wu, L. Ge, R. Mao, Numerical study on the heat transfer performance of mine ice-storage cooling device, Int. J. Heat Mass Tran. 223 (2024) 125255, https://doi.org/10.1016/j.ijheatmasstransfer.2024.125255.
[46] H. Waqas, M.A. Khan, M. Hussain, Z. Zhang, Thermal enhancement of phase change materials using nanoparticles and novel finned structures, Mater. Today Sustain. 32 (2025) 101222, https://doi.org/10.1016/j.mtsust.2025.101222.
[47] H. Waqas, M. Hussain, U. Manzoor, Q.M. Al-Mdallal, M.A. Abdallah, I.E. Elseesy, Enhanced melting performance of nano-mediated phase change material with rectangular and parallelogram fins for thermal energy storage, J. Comput. Des. Eng. 12 (2025) 155–166, https://doi.org/10.1093/jcde/qwaf026.
[48] S. Khalid, M. Hussain, H. Waqas, D. Liu, Enhancing thermal energy storage efficiency with nano-integrated phase change materials: machine learning-driven optimization via computational fluid dynamics, Int. Commun. Heat Mass Tran. 167 (2025) 109221, https://doi.org/10.1016/j.icheatmasstransfer.2025.109221.
[49] S. Zainab, M.A. Khan, Sharmeen, H. Waqas, Artificial neural network based enhanced thermal energy storage system for renewable energy using nano-particles, Case Stud. Therm. Eng. 73 (2025) 106586, https://doi.org/10.1016/j.csite.2025.106586.
[50] A. Shahraki, A. Tavakoli, M. Mohammadi, A. Ebrahimi, A. Kianifar, Enhancing the charging performance of a triplex-tube thermal energy storage system using fins and nanoparticles, Therm. Sci. Eng. Prog. 62 (2025) 103565, https://doi.org/10.1016/j.tsep.2025.103565.
[51] A. Tavakoli, J. Hashemi, M. Najafian, A. Ebrahimi, Physics-based modelling and data-driven optimisation of a latent heat thermal energy storage system with corrugated fins, Renew. Energy 217 (2023) 119200, https://doi.org/10.1016/j.renene.2023.119200.
[52] L. Yang, H. Wu, Z. Zhang, R. Mao, J. Zhou, X. Liang, Experimental investigation on application potential of phase change assisted direct ventilation cooling system for Gui'an data center, Appl. Therm. Eng. 254 (2024) 123932, https://doi.org/10.1016/j.applthermaleng.2024.123932.
[53] X. Li, H. Yang, R. Mao, H. Wu, X. Liang, J. Zhou, Z. Zhang, Experimental investigation on the temperature control performance of compressed air coupled phase change plate system for underground refuge chamber, Int. J. Heat Mass Tran. 233 (2024) 126028, https://doi.org/10.1016/j.ijheatmasstransfer.2024.126028.
[54] R. Ye, R. Huang, X. Fang, Z. Zhang, Simulative optimization on energy saving performance of phase change panels with different phase transition temperatures, Sustain. Cities Soc. 52 (2020) 101833, https://doi.org/10.1016/j.scs.2019.101833.
[55] Q. Li, J. Jiang, Y. Hong, J. Du, Numerical investigation of thermal management performances in a solar photovoltaic system by using the phase change material coupled with bifurcated fractal fins, J. Energy Storage 56 (2022) 106156, https://doi.org/10.1016/j.est.2022.106156.
[56] R. Tu, J. Li, Y. Hwang, Study of temperature uniformity and thermal storage performances of a shell-and-tube type phase change plate, Int. J. Refrig. 122 (2021) 69–80, https://doi.org/10.1016/j.ijrefrig.2020.11.001.
[57] H. Xu, J. Zhou, X. Liang, X. Yi, H. Wu, R. Mao, Z. Zhang, Enhancing the thermal performance of a phase change energy storage assisted ventilation system via unit structure optimization for data center, Int. Commun. Heat Mass Tran. 167 (2025) 109396, https://doi.org/10.1016/j.icheatmasstransfer.2025.109396.
[58] X. Gao, Y. Yuan, H. Wu, X. Cao, X. Zhao, Coupled cooling method and application of latent heat thermal energy storage combined with pre-cooling of envelope: optimization of pre-cooling with intermittent mode, Sustain. Cities Soc. 38 (2018) 370–381, https://doi.org/10.1016/j.scs.2018.01.014.
[59] R. Shaheed, A. Mohammadian, H. Kheirkhah Gildeh, A comparison of standard k–ε and realizable k–ε turbulence models in curved and confluent channels, Environ. Fluid Mech. 19 (2019) 543–568, https://doi.org/10.1007/s10652-018-9637-1.
[60] A.I.N. Korti, H. Guellil, Experimental study of the effect of inclination angle on the paraffin melting process in a square cavity, J. Energy Storage 32 (2020) 101726, https://doi.org/10.1016/j.est.2020.101726.
[61] H. Soltani, M. Soltani, H. Karimi, J. Nathwani, Heat transfer enhancement in latent heat thermal energy storage unit using a combination of fins and rotational mechanisms, Int. J. Heat Mass Tran. 179 (2021) 121667, https://doi.org/10.1016/j.ijheatmasstransfer.2021.121667.
[62] G. Feng, T. Wang, K. Huang, G. Wang, Y. Cheng, L. Zhang, A. Li, Simulation of a new phase change energy storage tank design with a vertical baffle, Energy Build. 268 (2022) 112205, https://doi.org/10.1016/j.enbuild.2022.112205.
[63] A. Ebrahimi, C.R. Kleijn, I.M. Richardson, Sensitivity of numerical predictions to the permeability coefficient in simulations of melting and solidification using the enthalpy-porosity method, Energies 12 (2019) 4360.
[64] Y. Yuan, X. Gao, H. Wu, Z. Zhang, X. Cao, L. Sun, N. Yu, Coupled cooling method and application of latent heat thermal energy storage combined with pre-cooling of envelope: method and model development, Energy 119 (2017) 817–833, https://doi.org/10.1016/j.energy.2016.11.058.
[65] T. Wu, W. Zhou, Z. Ling, Z. Zhang, X. Fang, Numerical simulation and optimization of a high-performance serpentine tube phase change cold storage unit based on high thermal conductivity ice/expanded graphite, Int. J. Heat Mass Tran. 238 (2025) 126497, https://doi.org/10.1016/j.ijheatmasstransfer.2024.126497.
[66] X. Huang, Z. Li, Y. Xie, J. Gao, X. Yang, M.-J. Li, Thermo-fluidic characteristics of contact melting mechanism for water-phase change material mixture: a numerical optimization, Int. J. Heat Fluid Flow 110 (2024) 109561, https://doi.org/10.1016/j.ijheatfluidflow.2024.109561.